Mechanical Systems and Signal Processing 227 (2025) 112400

Contents lists available at ScienceDirect

Mechanical Systems and Signal Processing

journal homepage: www.elsevier.com/locate/ymssp

3D sound radiation reconstruction from camera measurements

Sofia Baldini [a,*], Gianluca Guernieri [a], Domen Gorjup [b], Paolo Gardonio [a], Janko Slavič [b], Roberto Rinaldo [a]

[a] Università degli Studi di Udine – DPIA, Via delle Scienze 206, 33100 Udine, IT, Italy
[b] University of Ljubljana – Faculty of Mechanical Engineering, Askerceva 6 1000, Ljubljana, SI, Slovenia

ARTICLE INFO

Communicated by Efren Fernandez-Grande

Keywords:
Videogrammetry
Flexural vibration measurement
Sound radiation reconstruction
Frequency-domain triangulation

ABSTRACT

In general, the measurement of the sound radiation field by machinery and partitions requires time-consuming tests, which should be carried out in specially dedicated anechoic/reverberant facilities with calibrated sensors and complex acquisition and post processing equipment. This article introduces a two-step method for the identification from optical measurements of the free-field sound radiation generated by flexural vibrations of closed shells. In the first step, the flexural vibration of the shell is reconstructed with a frequency domain triangulation technique based on short multi-view video acquisitions made with a single high-resolution, high-speed camera. In the second step, the free-field sound radiation is derived from a discretized boundary integral formulation. The study is focused on the identification of the sound radiation from the flexural vibration of a baffled cylinder model structure. The vibration and sound fields reconstructed from the camera measurements are validated against direct measurements taken with a laser scanner vibrometer and a microphone array, respectively. Overall, this research demonstrates that optical methods based on camera measurements can be suitably employed to produce fast and accurate full-field measurements of sound radiation of closed shells (without the need for a dedicated measurement environment, e.g. reverberant, anechoic chambers).

1. Introduction

In general, the measurement of sound radiation by machinery or wall structures is carried out in specially dedicated facilities involving large reverberant and/or anechoic rooms [1,2] (see also the ISO[1] 3740:2019, 3741:2010, 3745:2012). These are rather costly facilities (both to fabricate and to run), which are normally available at certification and research centres that provide measurement services to third parties. In cases where it is difficult, or too expensive, to move the machinery or structure, sound radiation measurements are taken directly *in situ* where the equipment is installed [1,2] (see also the ISO 3740:2019, 3746:1996, 3747:2000), although this solution is rather delicate to perform since it should be arranged in such a way that the effects of sound reflections from walls or partitions and the effects of flanking noise generated by other machineries or plants be minimal.

The need for increasingly simpler and more practical approaches for the measurement of the sound radiation from machinery and partitions has led to quite a few prolific streams of research and technical development focused both on new measurement paradigms and on innovative sensors and measurement equipment as well as new acoustic facilities (for example small anechoic rooms [3], which

* Corresponding author.
E-mail address: baldini.sofia@spes.uniud.it (S. Baldini).

[1] International Organization for Standardization

https://doi.org/10.1016/j.ymssp.2025.112400
Received 11 June 2024; Received in revised form 25 November 2024; Accepted 23 January 2025
Available online 1 February 2025

can be equipped with active noise control systems that cancel low frequency sound reflections from the walls [4–7]). As recalled in Ref. [8], already in the 1930s, the idea of detecting nearfield sound intensity was considered a viable option for simple in situ measurements of the sound radiation by machinery and partitions, which does not require specially dedicated acoustic infrastructures [9]. Here, there is yet quite a lot of research work in progress, which involves the making and calibration of the probes [9,10] as well as the automatic acquisition and reconstruction of the sound intensity field [11]. Alongside acoustic intensity measurements, nearfield acoustic holography too has been the subject of many studies to detect sound radiation [12]. For instance, compressive nonstationary near-field acoustic holography has been used to reconstruct instantaneous sound fields [13,14]. Moreover, a hybrid nearfield acoustic holography has been proposed to reconstruct the sound radiation by sources with irregular geometries [15]. Besides, deep learning techniques have been applied to enhance the quality of sound field reconstruction [16]. In parallel, far field methods based on microphone arrays (also known as acoustic cameras) are the subject of intensive research too. These methods rely on microphone arrays and, in some cases, a dish scatterer to detect the source of noise with beamforming methods [17–19]. Here, the research work has been focused on the design of compact omnidirectional sound cameras using the three-dimensional acoustic intensimetry [20]. Also, there has been quite a lot of activity on the acoustic imaging combing object detection with conventional frequency domain beamforming [21,22]. Moreover, direction-of-arrival algorithms have been developed [23], as well as, new methods for estimating the sound radiation by moving objects [24].

In parallel to direct acoustic measurements, taking inspiration from the Kirchooff – Helmholtz formulation for the sound radiation of vibrating structures [25–28], Rohlfing *et al.* [29] reconstructed the sound radiation produced by the flexural vibration of a flat panel using point measurements taken with a scanning laser vibrometer. More precisely, they divided the surface of the panel into a regular grid of elementary radiators [28,30] and measured the transversal velocity at their centers with the vibrometer such that the sound radiation could then be calculated with a discretized version of the Kirchooff – Helmholtz integral equation [25–28], which, for a plane baffled radiator, boils down to the Rayleigh integral [25–28]. This idea was taken forward in Refs. [31,32] to derive the sound radiation of structures in terms of radiation modes, which, as shown in [28], provide more insights into the phenomenon of sound radiation itself.

Recently, Gardonio *et al.* [33–35] have proposed to employ full field camera measurements to reconstruct the sound radiation produced by the flexural vibration of structures. Their idea resembles the elemental radiators technique discussed above, except that the vibration field is measured with optical cameras [36] rather than a scanner laser vibrometer [29,31,32]. With this approach, the acoustics of the measurement room, as well as flanking sources or background noise, have no direct effect on the reconstruction of the sound field. In principle they can influence the vibration of the structure and thus indirectly the sound radiation, but this effect is expected to be negligible for sound radiation in air and in large spaces with low reverberation as well as for typical flanking sources and background noise that may be encountered in practice. This is quite a relevant advantage since it is expected that the proposed method can be suitably implemented for *in situ* measurements without the need of moving the tested equipment into anechoic rooms. Moreover, the camera acquisitions provide fast full-field vibration measurements such that the sound radiation can be estimated with denser grids of elements and thus greater accuracy of the sound radiation prediction. Also, the experimental work presented in Ref. [34] has showed that, contrary to the measurements taken with the scanning laser vibrometer, rather short video acquisitions are required to reconstruct the whole vibration field. Thus, the measurement is carried out in nominal ambient conditions with no variations of the dynamic response of the structure being tested.

During the past three decades, vibration measurements using optical cameras has been the subject of quite a few studies [36], both because of their high spatial resolution and because of their non-contact nature, which is essential when dealing with lightweight structures. Different approaches to reconstructing displacements from images have been used, including 2D-Point-Tracking (2DPT) [37,38] and 3D-Point-Tracking (3DPT) [39] techniques as well as the Digital-Image-Correlation (DIC) method [40,41]. More computationally efficient techniques, such as the simplified optical flow method [42] are also available when fast postprocessing is required. To measure 3D vibrations using 2D digital images, at least two camera views, observing matching points of interest, are required. This is often achieved using a synchronized pair of high-speed cameras and the well-established 3D DIC technique [40]. To avoid possible synchronization and optical errors in multi-camera setups, the so-called single-camera multi-view methods are currently studied actively. These methods often utilize additional optical elements such as mirror systems to project multiple views of the structure surface onto a single camera sensor, reducing the measurement resolution as a result [43]. The frequency-domain triangulation method [44] is another technique that enables the use of a single camera for spatial vibration measurements, which, exploits full image-sensor resolution. It can be implemented with a still-frame camera and does not require synchronization of multiple cameras [45].

This paper proposes a general method for the measurement of sound radiation produced by the flexural vibration of 3D closed shell structures, which is based on frequency domain triangulation of multi-view optical recordings taken with a single camera. The method relies on a fixed high-speed camera that takes multi-view recordings of the cylinder model structure, which is suitably rotated around its principal axis in between acquisitions. More specifically, it implements a two steps procedure where, first, the flexural vibration field is reconstructed via frequency-domain triangulation of multi-view camera acquisitions [44], and, second, the sound radiation field is derived from a discretised Kirchooff – Helmholtz integral [25–28].

The article is organized in three parts. To start with, Section 2 describes the model structure and the test rig considered in this work, which, to provide a simple, but realistic, case study, was chosen as a thin walled, baffled, cylinder excited in bending by a radial point force. Then, Section 3 introduces the new method proposed for the reconstruction from camera measurements of 3D sound radiation. Finally, Section 4 shows experimental results where the proposed method has been employed to reconstruct the sound radiation fields generated by the time-harmonic flexural vibrations of the baffled thin-walled cylinder. The vibration and acoustic fields derived from the optical measurements are validated against direct measurements taken with a scanner laser vibrometer and a microphone array

respectively.

2. Model structure and measurement setups

As anticipated above, to have a simple and representative case study, both for the reconstruction of the 3D flexural vibration from triangulation of multiple optical images and for the analytical derivation of the sound radiation with the Kirchhoff-Helmholtz integral, the thin-walled baffled cylinder model structure described in Subsection 2.1 below was chosen. In this way, the optical measurements were taken with a single camera setup, which, as discussed in the following Subsection 2.2, employed a high speed and high spatial resolution camera. Also, to validate the proposed methodology, the laser vibrometer and microphone array setups described in the final Subsection 2.3 were used to measure the vibration and acoustic fields respectively.

2.1. Thin-walled baffled cylinder model-structure and measurement approach

Fig. 1 shows three sketches of the thin-walled cylinder considered in this study, which is made of steel and has thickness $h = 1$ mm, radius $R = 149$ mm and height H = 296 mm. The cylinder is clamped on rigid flanges at the two ends and is also equipped with two cylindrical extensions, which work as acoustic rigid baffles. In this way, the sound radiation generated by the flexural vibration of the baffled cylinder can be suitably derived from analytical formulations [26]. For more complex geometries, Boundary Element Method (BEM) or Finite Element Method (FEM) numerical approaches should be employed [28]. As will be described in detail in Section 3, in this study, the Frequency Response Functions (FRFs) of the radial displacements per unit force excitation were first reconstructed from camera measurements with a frequency domain triangulation technique [46] at the grid of $62 \times 20 = 1240$ target points, which, as shown in Fig. 1b, were located at the centres of the mesh of quadrangular elements used for the derivation of the sound radiation. Then, as highlighted in Fig. 1b,c, the FRFs of the radiated sound pressure per unit force excitation were derived with a discretized version of the Kirchooff – Helmholtz integral [25–28] at a grid of $24 \times 14 = 336$ points laying on a horizontal plane that cuts into two sections the cylinder and at two grids of $12 \times 14 = 168$ laying on a vertical plane that cuts into two halves the cylinder. More specifically, the FRFs of the sound pressure per unit force excitation at each point in the outer acoustic domain were derived with a midpoint-Riemann sum of the Kirchhoff – Helmholtz integral based on the mesh of quadrangular elements depicted in Fig. 1b [35]. Considering the physics of the sound radiation phenomenon, this corresponds to accounting for the superposition of the sound radiated by the radial vibration of the mesh of quadrangular elements, assuming each element vibrates in a rigid cylindrical baffle of infinite length [26,28]. Here, the sound radiation by a small piston that vibrates on an infinitely long rigid cylinder can be suitably derived with analytical expressions as shown in Refs. [47–49] for example (these papers provide seemingly different expressions simply because they refer to time-harmonic functions given in either complex forms $e^{\pm j\omega t}$, where ω is the circular frequency).

The time-harmonic flexural vibration and sound radiation fields per unit force excitation were then reconstructed from the vibration and sound radiation FRFs. They were therefore represented considering a fixed instant of time in which the amplitude of the flexural vibrational field of the cylinder is maximum. The time-harmonic vibration and acoustic fields were derived at four resonance frequencies of the cylinder flexural vibration, that is at $f_1 = 618$ Hz, $f_2 = 659$ Hz, $f_3 = 964$ Hz and $f_4 = 1231$ Hz. As will be shown below, in the 500 – 1500 Hz frequency range considered in this study, the flexural response of the cylinder is characterised by a low modal overlap [50] such that, at resonance frequencies, the flexural vibration of the cylinder is mostly controlled by the resonant flexural mode. Hence, considering a time instant where the amplitude of the vibration is maximum, the flexural field closely reproduces the shape of the resonant mode, which is normally called "Operating Deflection Shape" (ODS) [51]. Likewise, the acoustic field radiated in the proximity of the cylinder, i.e. the acoustic nearfield, is characterised by distinct lobes that replicates the circular shape of the flexural mode that controls the resonant response, that is the operating deflection shape, at the given resonance frequency. For the resonance frequency $f_4 = 1231$ Hz, the map was reconstructed at 3/4 of the cylinder height since the vibration field was characterised by a nodal line at the midspan of the cylinder. In fact, given the symmetry of the vibration field, the sound radiation at

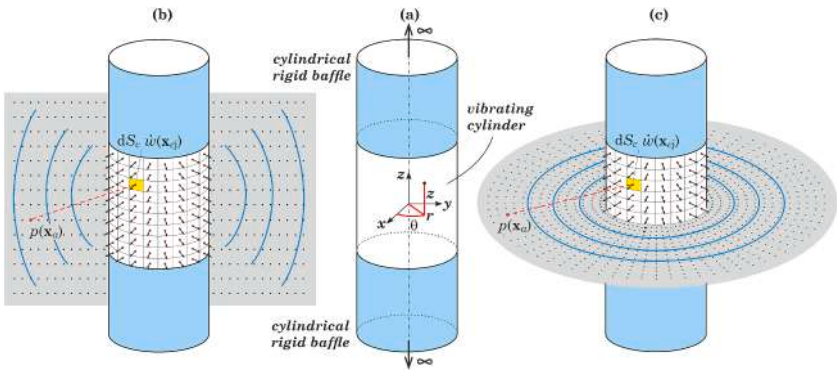

Fig. 1. (a) Baffled cylinder and derivation of the sound fields in (b) vertical and (c) horizontal planes from the radiations of a mesh of quadrangular pistons in the rigid cylindrical baffle.

the mid-plane would show a very small uniform distribution of the sound pressure due to mutual cancellation effects from the anti-symmetric radiations produced by the vibrations of the top and bottom half of the cylinder.

2.2. Test rig and camera measurement setup

Fig. 2 shows the baffled cylindrical model structure built for this study. As can be noticed in Fig. 2b, the cylinder was fixed on two flanges such that it can be considered clamped at the two terminations. Also, as shown in Fig. 2a, two cylindrical extensions were fixed at the bottom and top side of the cylinder, which had been closed with circular disks. The bottom disk was mounted on a base flange via a turning joint such that the whole baffled cylinder could be rotated during the measurement campaigns while the optical camera and the laser vibrometer were kept fixed. Fig. 2b,c show the high-contrast speckle pattern, applied to the cylinder surface to facilitate the Digital Image Correlation image-processing stage. Two rows of ArUco markers were printed at the top and bottom of the pattern for the automatic extrinsic calibration of the multi-view imaging system.

The cylinder was rotated around its vertical axis between consecutive video acquisitions. In this way, high-speed camera footage of the cylinder under stationary broadband random excitation was acquired from 18 different viewpoints, using the same excitation signal in each measurement. The Photron FASTCAM SA-Z high-speed optical camera shown in Fig. 2a was used to measure 50.000 12-bit monochrome images at 10.000 frames-per-second, with the spatial resolution of 896 $\times$ 896 pixels for each viewpoint, producing 1.31 terabytes of image-data in total.

The calibration of the multi-view images was performed in two stages. Firstly, images of a standard checkerboard calibration pattern were used to perform the intrinsic camera calibration, to give reference optical parameters such as the focal length and the optical centre of the camera, which are then incorporated in the so-called intrinsic camera calibration matrix $\mathbf{K}$ [52]. As the camera optical settings were unchanged during the whole image acquisition process, this step was performed only once. Secondly, the ArUco makers in the recorded images were combined with their known positions on the cylinder surface to perform the extrinsic camera calibration for each of the 18 viewpoints using the Perspective-n-Point algorithm [53]. In this way, the perspective camera rotation matrices $\mathbf{R}$ and translation vectors $\mathbf{t}$ were also derived for each viewpoint i, giving a fully calibrated multi-view imaging system, with known perspective camera projection matrices $\mathbf{P}_i$ [54]:

$$\mathbf{P}_i = \mathbf{K}[\mathbf{R}_i|\mathbf{t}_i] \tag{1}$$

2.3. Laser vibrometer and microphone array measurement setups

The vibration and sound radiation fields reconstructed from the camera measurements were validated against measurements taken respectively with the laser vibrometer and the microphones array shown in Fig. 3a and 3b,c respectively. To this end, as can be noticed in Fig. 2c, the speckle pattern decal applied on to the cylinder was enhanced with a grid of green circular markers that served as target points for the measurements with the laser vibrometer. The markers were located at the centres of the regular grid of quadrangular elements depicted in Fig. 1b. The flexural vibrations at the whole set of markers were measured with the laser vibrometer oriented in such a way as its vertical measurement plane went through the vertical axis of the cylinder. More specifically, the laser automatically scanned the vibrations of the array of markers aligned with the laser vertical plane of measurement and then the cylinder was rotated in such a way as to measure the neighbouring vertical array of markers and so on. The laser vibrometer detected the spectra of the mobility FRFs for the radial velocities per unit force excitation of the shaker located inside the cylinder.

The sound field on the vertical measurement plane was measured at the two grids of $12 \times 14 = 168$ points depicted in Fig. 1b with the vertical array of microphones depicted in Fig. 3b, which were suitably translated in radial direction to get the whole field. Also, the sound field on the horizontal measurement plane was measured at the grid of $11 \times 104 = 1144$ points depicted in Fig. 1c with the radial array of microphones shown in Fig. 3c. Here, considering Fig. 4b, as done for the vibration measurements with the laser vibrometer, the microphones array was aligned along a radial segment and kept in the same position whereas the cylinder was rotated

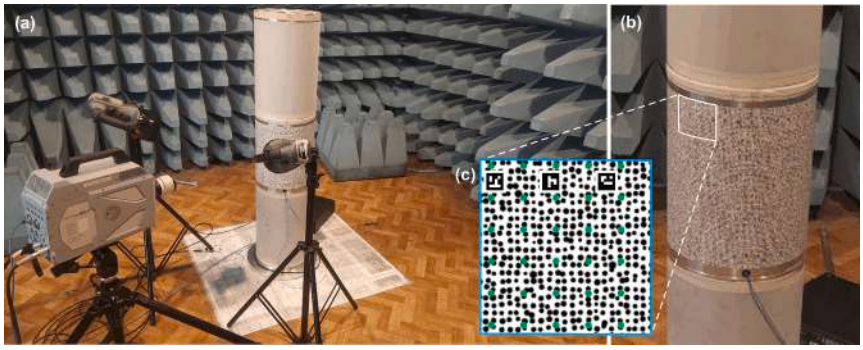

Fig. 2. (a) optical camera measurement setup, (b) cylinder with the speckled surface, (c) details of the speckle pattern for the camera (black dots) and laser (green dots) measurements. (For interpretation of the references to colour in this figure legend, the reader is referred to the web version of this article.)

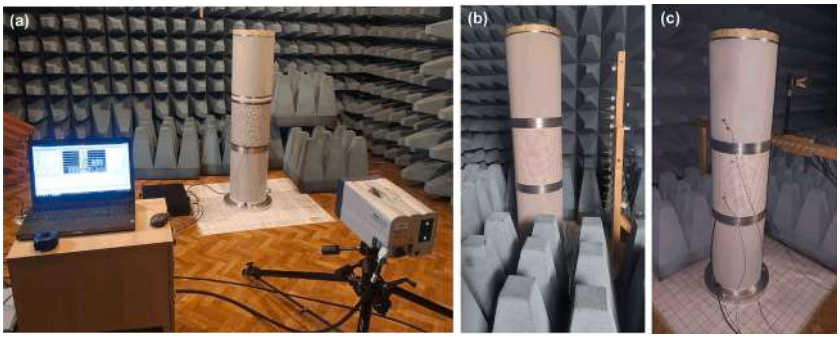

Fig. 3. laser vibrometer (a) and microphone array measurement setups for the vertical (b) and horizontal (c) plane maps.

by 360 deg to get the whole field. The measurements were carried out in a 500 – 1500 Hz frequency range such that the acoustic wavelength spanned in the range comprised between 0.69m and 0.23m. Hence, the maps depicted in great details the lobes due to the near field sound radiation generated by the flexural vibration of the cylinder [28].

3. 3D sound radiation reconstruction from camera measurements

The approach proposed for the measurement of the flexural vibration and sound radiation fields from multiple images recordings is now presented. To start with, this section describes in detail the measurement procedure with the optical camera setup presented in Section 2.2 and shown in Fig. 2, as well as the frequency domain triangulation from multi-view image acquisitions implemented to detect the radial displacements of the grid of marker points. Next, it briefly recalls the derivation of the operation deflection shapes that characterise the flexural vibration field at given frequencies. Finally, it describes in detail the integral formulation employed to derive the sound pressure fields based on a Riemann sum of the Kirchhoff – Helmholtz integral expression [35].

3.1. Frequency-domain triangulation for single-camera 3D-FRF measurement

As anticipated above, in this study, the flexural vibrations of the cylinder are derived from digital images taken with a single camera using the frequency-domain triangulation method introduced in Ref. [44]. This method reconstructs with a single camera the whole vibration field of the structure. In contrast to classical camera vibration measurement methods [36], the multi-view triangulation implemented in this work is not based on simultaneous recordings taken with multiple cameras from different viewpoints [55], but instead on consecutive recordings taken with a single camera while the structure is rotated between each recording and is forced by the same stationary excitation. The measurements are taken with small-amplitude excitations that guarantee a linear response of the

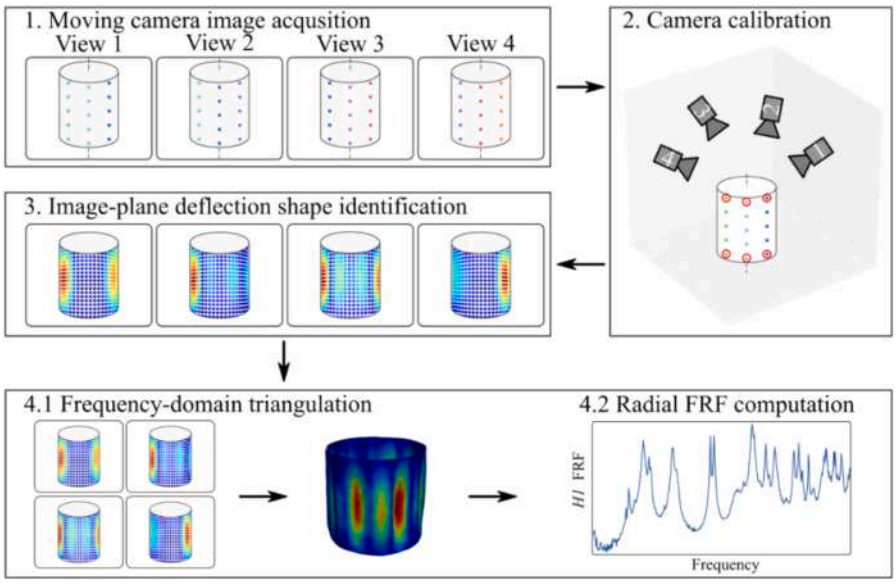

Fig. 4. The image-based 3D displacement measurement procedure using frequency-domain triangulation and the single-camera multi-view approach.

structure. The image-based displacements provided by each recording are then transformed into the frequency-domain to generate the spectra of the physical displacements with a frequency-domain triangulation [44]. It is important to stress the fact that the sequence of multi-view recordings is taken with separate experiments requiring only a given stationarity excitation between consecutive measurements. The frequency-domain triangulation method is capable of reconstructing spatial operating deflection shapes (ODS) of linear, time-invariant systems under stationary excitation using a single, moving camera, assuming small-amplitude harmonic displacements.

Overall, the method employed in this study can be summarized by the following steps, which are illustrated in Fig. 4:

1. Image acquisition, using a moving specimen (see Section 2.2).
2. Multiview imaging system calibration (see Section 2.2).
3. 2D image-based displacement FRFs identification using Lucas-Kanade DIC [56].
4. Frequency-domain multi-view triangulation and computation of dynamic flexibility FRFs.

The principal steps of this procedure are hereby recalled and then expanded to provide the incipit for the subsequent derivation of the vibration and sound radiation fields due to tonal excitations. The details of the whole formulation of the frequency-triangulation method can be found in Ref. [44].

The process of acquiring images using a perspective camera $\mathbf{P}$ can be described by a projective mapping, where an arbitrary point (x, y, z) in space defined by the homogeneous vector $\mathbf{x} = (x, y, z, 1)^T$ is mapped by the projection matrix $\mathbf{P}$ defined in Eq. (1) into its 2D image (x', y') defined by the homogeneous vector $\mathbf{x}' = (x', y', 1)^T$:

$$\mathbf{x}' = \frac{1}{w}\mathbf{P}\mathbf{x} \tag{2}$$

Hereafter the symbol $'$ is used to specify a position or displacement in the image space. This mapping is linear in the projective space, but non-linear in the Euclidean space, due to the perspective scale factor w, which depends on both the projection matrix $\mathbf{P}$ as well as the position of the observed point $\mathbf{x}$ [54]. As a result, in general, multiple points in space can be projected onto the same image point, and this makes the perspective camera projection non-invertible. However, if the same point in space is observed from at least two distinct viewpoints, this information can be used to univocally reconstruct its 3D position $\mathbf{x}$ in a process called triangulation [54].

Here, the aim is to use frequency-triangulation of image-based data to reconstruct the dynamic flexibility FRFs between the cylinder radial displacements at the grid of markers and the radial force exerted on the cylinder. To this end, the time-harmonic radial displacement and radial force are expressed as

$$u_r(\mathbf{x}_{cj}, t) = \mathrm{Re}\{u_r(\mathbf{x}_{cj}, \omega)e^{j\omega t}\} \tag{3}$$

$$f_r(\mathbf{x}_{cf}, t) = \mathrm{Re}\{f_r(\mathbf{x}_{cf}, \omega)e^{j\omega t}\} \tag{4}$$

where ω is the circular frequency, $j = \sqrt{-1}$, and $u_r(\mathbf{x}_{cj}, \omega), f_r(\mathbf{x}_{cf}, \omega)$ are respectively the complex amplitude of the radial displacement at the j-th marker position $\mathbf{x}_{cj}$ and the complex amplitude of the time-harmonic radial force excitation at position $\mathbf{x}_{cf}$. The dynamic flexibility FRFs between the radial displacement of the marker points and force excitation are thus given by

$$\alpha_{rj}(\omega) = \frac{u_r(\mathbf{x}_{cj}, \omega)}{f_r(\mathbf{x}_{cf}, \omega)} \tag{5}$$

The objective of the frequency-triangulation is to derive the complex amplitudes of the time-harmonic radial displacements at the centres of the quadrangular elemental radiators. Hence, a relation should be established in the form of the perspective camera projection given in Eq. (2) between the complex amplitudes of the marker displacements and the complex amplitudes of their image projections.

In general, for the j-th marker point depicted on the cylinder, which vibrates harmonically with respect to a rest (i.e. reference) position defined with the vector $\mathbf{x}_{cjREF}$, the displacement in the image space is given by the vector:

$$\mathbf{u}'_{cj}(t) = \frac{1}{w(t)}\mathbf{P}\mathbf{x}_{cj}(t) - \frac{1}{w_{REF}}\mathbf{P}\mathbf{x}_{cjREF} \tag{6}$$

here the vector $\mathbf{x}_{cj}(t)$, specifies the position of the marker at time t whereas the vector $\mathbf{u}'_{cj}(t)$ contains the two components of the displacement in the image plane at time t. For small time-harmonic displacements, the perspective scale factor at time t can be assumed equal to that for the reference position of the marker, that is $w(t) = w_{REF}$, such that the equation above becomes

$$\mathbf{u}'_{cj}(t) = \frac{1}{w_{REF}}\mathbf{P}(\mathbf{x}_{cj}(t) - \mathbf{x}_{cjREF}) \tag{7}$$

As reported in Ref. [44], to derive the complex amplitude of the image-based displacement, the discrete Fourier transform is applied to Eq. (7) considering N images:

$$\mathbf{u}'_{cj}(\omega) = \frac{1}{w_{REF}}\mathbf{P}\frac{1}{N}\sum_{n=0}^{N-1}\left(\mathbf{x}_{cj}(t_n) - \mathbf{x}_{cjREF}\right)e^{-\mathrm{j}2\pi nk/N} \tag{8}$$

here the vector $\mathbf{u}'_{cj}(\omega)$ contains the complex amplitudes of the two components of the time-harmonic displacement in the image plane. To retrieve the displacement vector in the 3D Euclidean space, the displacement in the image plane should be translated back to its reference position in the image space, such that, as shown in Ref. [44], the following relation holds

$$\mathbf{u}'_{cj}(\omega) + \mathbf{x}'_{cjREF} = \frac{1}{w_{REF}}\mathbf{P}\left(\mathbf{u}_{cj}(\omega) + \mathbf{x}_{cjREF}\right) \tag{9}$$

In this case, the vector

$$\mathbf{x}_{cj}(\omega) = \mathbf{u}_{cj}(\omega) + \mathbf{x}_{cjREF} \tag{10}$$

contains the complex amplitudes of the three components of the marker position in the Euclidean space, which, as shown in Ref. [44] can be used to implement a multi-view triangulation in the frequency-domain that leads to a univocal displacement vector $\mathbf{u}_{cj}(\omega)$.

To retrieve the receptance FRF defined in Eq. (5), the complex amplitude of the radial component of the displacement is extracted from the vector $\mathbf{u}_{cj}(\omega)$ with the following projection

$$u_r\left(\mathbf{x}_{cj},\omega\right) = \frac{\mathbf{u}_{cj}(\omega)\cdot\mathbf{n}_j}{\left|\mathbf{n}_j\right|} \tag{11}$$

where $\mathbf{n}_j$ is the unit vector normal to the surface of the cylinder at the marker position $\mathbf{x}_{cj}$. As done for the displacements, the complex amplitude of the force excitation is derived with a discrete Fourier transform of the force time recording considering N samples

$$f_r\left(\mathbf{x}_{cf},\omega\right) = \frac{1}{N}\sum_{n=0}^{N-1} f_r\left(\mathbf{x}_{cf},t_n\right)e^{-\mathrm{j}2\pi nk/N} \tag{12}$$

3.2. Reconstruction of the flexural vibration field

Assuming time-harmonic vibrations, the flexural vibration field of the cylinder at given frequencies ω has been reconstructed and depicted in terms of the operational deflection shapes, which can be derived from Eq. (3) rewritten in the following trigonometric form:

$$u_r\left(\mathbf{x}_{cj},t\right) = U_r\left(\mathbf{x}_{cj},\omega\right)\cos\left(\omega t + \varphi_U\left(\mathbf{x}_{cj},\omega\right)\right) \tag{13}$$

Here $U_r\left(\mathbf{x}_{cj},\omega\right) = \left|\alpha_{rj}(\omega)f_r\left(\mathbf{x}_{cf},\omega\right)\right|$ and $\varphi_U\left(\mathbf{x}_{cj},\omega\right) = \angle\left\{\alpha_{rj}(\omega)f_r\left(\mathbf{x}_{cf},\omega\right)\right\}$ are respectively the amplitude and phase of the displacement at each marker point. For synchronous vibrations, the deflection shapes show the typical stationary fields characterised by positive and negative lobes. The operational deflection shapes can thus be retrieved from Eq. (13) considering an instant of time such that the vibration field reaches its maximum amplitude, that is when $\left|\cos\left(\omega t + \varphi_U\left(\mathbf{x}_{ci},\omega\right)\right)\right| = 1$. In general, the deflection shape of a structure at a resonance frequency well separated from neighbouring resonance frequencies, such that the flexural response is controlled by the resonant mode, can be suitably obtained from the real part of the complex amplitude, that is $\mathrm{Re}\left\{u_r\left(\mathbf{x}_{cj},\omega\right)\right\}$. To conclude, it should be highlighted that, when the laser vibrometer measurements were employed to derive the flexural deflection shapes, then the formulation presented in this section was employed setting:

$$\alpha_{rj}(\omega) = \frac{Y_{rj}(\omega)}{j\omega} \tag{14}$$

where

$$Y_{rj}(\omega) = \frac{v_r\left(\mathbf{x}_{cj},\omega\right)}{f_r\left(\mathbf{x}_{cf},\omega\right)} \tag{15}$$

are the mobility functions measured by the laser vibrometer. Here, $v_r\left(\mathbf{x}_{cj},\omega\right) = j\omega u_r\left(\mathbf{x}_{cj},\omega\right)$ is the complex amplitude of the radial velocity at the marker position; which is given by:

$$v_r\left(\mathbf{x}_{cj},t\right) = \mathrm{Re}\left\{v_r\left(\mathbf{x}_{cj},\omega\right)e^{j\omega t}\right\} \tag{16}$$

3.3. Reconstruction of the sound radiation field

As discussed in Section 2.1 and shown in Fig. 1b,c, the radiated sound field has been reconstructed in a vertical plane that cuts in two halves the cylinder and in a horizontal plane that cuts in two sections the cylinder. Hence, as shown in Fig. 4, the sound pressure was derived at a dense grid of points with coordinates $\mathbf{x}_{ai} = \left(r'_i,\theta'_i,z'_i\right)$. The acoustic pressure $p(\mathbf{x}_{ai},t)$ at position $\mathbf{x}_{ai}$ was reconstructed considering the Kirchooff – Helmholtz integral expression for the sound radiation in free-field by a vibrating body [25–28]. More

specifically, assuming time-harmonic vibrations, and thus time-harmonic sound radiation, the sound pressure was taken equal to

$$p(\mathbf{x}_{ai},t) = \mathrm{Re}\{p(\mathbf{x}_{ai},\omega)e^{j\omega t}\} \tag{17}$$

where $p(\mathbf{x}_{ai},\omega)$ is the frequency-dependent complex amplitude at position $\mathbf{x}_{ai}$ which was calculated from the following Kirchhoff – Helmholtz integral expression:

$$p(\mathbf{x}_{ai},\omega) = -\int_{S_c}\left(p(\mathbf{x}_c,\omega)\frac{\partial g(|\mathbf{x}_{ai}-\mathbf{x}_c|,\omega)}{\partial r}+j\omega\rho_0 g(|\mathbf{x}_{ai}-\mathbf{x}_c|,\omega)v_r(\mathbf{x}_c,\omega)\right)dS_c \tag{18}$$

here ρ_0 is the density of air and S_c encompasses the surfaces of the flexible thin-walled cylinder as well as the surfaces of the two rigidly walled cylindrical baffles. Also, $v_r(\mathbf{x}_c,\omega)$ is the complex amplitude of the radial velocities at position $\mathbf{x}_c$ and $g(|\mathbf{x}_{ai}-\mathbf{x}_c|,\omega)$ is the free-space 1st-kind Green's function,

$$g(|\mathbf{x}_{ai}-\mathbf{x}_c|,\omega) = \frac{e^{jk|\mathbf{x}_{ai}-\mathbf{x}_c|}}{4\pi|\mathbf{x}_{ai}-\mathbf{x}_c|} \tag{19}$$

As highlighted in Refs. [26,57,58], this function gives the sound pressure at position $\mathbf{x}_{ai} = (r_i',\theta_i',z_i')$ generated by a point source (i.e. a monopole source with significantly smaller dimension than the acoustic wavelength) at position $\mathbf{x}_c = (R,\theta,z)$ on the cylinder. It is important to note that this Green's function depends on the distance between the two positions and not on their positions. The integral Eq. (18) refers to the complex amplitude of the radial velocity of the cylinder, $v_r(\mathbf{x}_c,\omega)$, as well as the complex amplitude of the acoustic pressure, $p(\mathbf{x}_c,\omega)$, which develops on the surface of the flexible cylinder and rigid baffles. The solution of this integral is thus not straightforward and requires a two steps procedure as discussed in Ref. [28] for example. Moreover, normally, the integration over the boundary surface cannot be solved analytically except when a Green's function $G(|\mathbf{x}_{ai}-\mathbf{x}_c|,\omega)$ can be constructed in such a way as to satisfy Neumann's boundary condition, that is $\partial G(|\mathbf{x}_{ai}-\mathbf{x}_c|,\omega)/\partial r = 0$ on the surface of the cylinder and baffles (as specified in [26,57,58], the Neumann boundary condition implies that the sound radiation from the elemental source be scattered by the boundary surface of the flexible cylinder and two baffles as if they were rigid walls). In this case the unknown sound pressure on the boundary surface $p(\mathbf{x}_c,\omega)$ vanishes and the integral in the Kirchhoff – Helmholtz equation simplifies into the following expression:

$$p(\mathbf{x}_{ai},\omega) = -j\omega\rho_0\int_{S_c}(G(|\mathbf{x}_{ai}-\mathbf{x}_c|,\omega)v_r(\mathbf{x}_c,\omega))dS_c \tag{20}$$

In general, this integral can be suitably solved analytically provided the boundary surface can be defined with respect to a single coordinate of a specific coordinate system (e.g. cylindrical coordinates in this case) and the acoustic wave equation is separable in such coordinate system [26]. This is indeed the case for the baffled cylinder vibrating structure considered in this study, for which the following analytical solution can be derived with respect to the cylindrical coordinate system R,θ,z [47–49]:

$$p(\mathbf{x}_{ai},\omega) = -j\frac{\omega\rho_0}{4\pi^2}\int_0^{2\pi}\int_0^{L}v_r(R,\theta,z,\omega)\sum_{n=-\infty}^{+\infty}\cos\left(n\left(\theta_i'-\theta\right)\right)I_n\left(z_i'-z\right)d\theta dz \tag{21}$$

where

$$I_n\left(z_i'-z\right) = \int_{-\infty}^{+\infty}\frac{\cos\left(k_z\left(z_i'-z\right)\right)}{k_rR}\frac{H_n^{(2)}\left(k_rr_i'\right)}{H_n^{(2)'}\left(k_rR\right)}dk_z \tag{22}$$

In these equations, $k=\omega/c$ is the acoustic wavenumber and c is the speed of sound in air. Also, k_z is the projection of the acoustic wavenumber into the longitudinal direction of the cylinder and $k_r = \sqrt{k^2-k_z^2}$. Finally, $H_n^{(2)}, H_n^{(2)'}$ are the 2nd-kind Hankel function and its derivative respectively [59]. Eq. (22) holds for time dependence taken in the complex form $e^{j\omega t}$ (if $e^{-j\omega t}$ was assumed to describe the co-sinusoidal time-harmonic vibration, then Eq. (21) would have had in front a term $+j$ and would have encompassed the 1st-kind Hankel function and therein derivative, that is $H_n^{(1)}$ and $H_n^{(1)'}$ respectively [59].

Since the radial velocity is reconstructed with the camera measurements at the grid of points shown in Fig. 1b,c, the surface integral in Eq. (21) has been calculated numerically with a middle Riemann sum considering the mesh of quadrangular radiators defined on the surface of the cylinder such that:

$$p(\mathbf{x}_{ai},\omega) \approx -j\frac{\omega\rho_0 S_e}{4\pi^2}\sum_{j=1}^{N_e}v_r\left(\mathbf{x}_{cj},\omega\right)\sum_{n=-\infty}^{+\infty}\cos\left(n\left(\theta_i'-\theta_j\right)\right)I_n\left(z_i'-z_j\right) \tag{23}$$

In this equation, S_e and N_e indicate the area and the number of the surface elements, whose centers are identified by the coordinates $\mathbf{x}_{cj} = \left(R,\theta_j,z_j\right)$. After a few mathematical steps, this equation can be further simplified into the following expression

$$p(\mathbf{x}_{ai},\omega) \approx -j\frac{\omega\rho_0 S_e}{2\pi^2}\sum_{j=1}^{N_e}v_r\left(\mathbf{x}_{cj},\omega\right)\sum_{n=0}^{N}\varepsilon_n\cos\left(n\left(\theta_i'-\theta_j\right)\right)\widehat{I}_n\left(z_i'-z_j\right) \tag{24}$$

where $\varepsilon_n = 1$ for $n = 0$, $\varepsilon_n = 2$ for $n > 0$, and the infinite summation is approximated into the sum of the first $N+1$ terms $\widehat{I}_n$

$$\widehat{I}_n(z_i' - z_j) = \int_0^{\infty} \frac{\cos(k_z(z_i' - z_j))}{k_r R} \frac{H_n^{(2)}(k_r r_i')}{H_n^{(2)'}(k_r R)} dk_z \tag{25}$$

Note that when $k_z > k$, $k_r = \sqrt{k^2 - k_z^2}$ becomes imaginary, and, in this case, it was set (see [59])

$$\frac{H_n^{(2)}(k_r r_i')}{k_r R H_n^{(2)'}(k_r R)} = \frac{K_n(|k_r| r_i')}{|k_r| R K_n'(|k_r| R)} \tag{26}$$

where K_n denotes the modified Bessel function of the second kind. The integral in Eq. (25) was approximated into a middle Reimann sum too, such that

$$\widehat{I}_n(z_i' - z_j) \approx \sum_{m=0}^{M} \frac{\cos(m\Delta k_z(z_i' - z_j))}{\sqrt{k^2 - (m\Delta k_z)^2} R} \frac{H_n^{(2)}\left(\sqrt{k^2 - (m\Delta k_z)^2} r_i'\right)}{H_n^{(2)'}\left(\sqrt{k^2 - (m\Delta k_z)^2} R\right)} \Delta k_z \tag{27}$$

here Δk_z and M were selected to achieve a reasonable approximation of the integral, as specified in Appendix A which reports the MatLab code that has been developed and used in this study to generate the acoustic maps presented into the forthcoming section.

Overall, the complex amplitude of the time-harmonic sound pressure at the i-th position generated by the radial vibration of the j-th quadrangular element was suitably expressed as follows

$$p(\mathbf{x}_{ai}, \omega) = Z_{ij}(\omega) v_r(\mathbf{x}_{cj}, \omega) \tag{28}$$

where, according to Eq. (24),

$$Z_{ij}(\omega) = -\mathrm{j} \frac{\omega \rho_0 Se}{2\pi^2} \sum_{n=0}^{N} \varepsilon_n \cos(n(\theta_i' - \theta_j)) \widehat{I}_n(z_i' - z_j). \tag{29}$$

Now, recalling that $v_r(\mathbf{x}_{cj}, \omega) = j\omega u_r(\mathbf{x}_{cj}, \omega)$ and using Eq. (5) into Eq. (28) gives

$$p(\mathbf{x}_{ai}, \omega) = j\omega Z_{ij}(\omega) \alpha_{rj}(\omega) f_r(\mathbf{x}_{cf}, \omega) \tag{30}$$

In conclusion, as seen for the flexural vibration field in Section 3.2, for time-harmonic vibrations, the sound radiation field of the cylinder at given frequencies ω can also be reconstructed and depicted in terms of "operational acoustic shapes", which can be derived from Eq. (17) rewritten in the following trigonometric form:

$$p(\mathbf{x}_{ai}, t) = P(\mathbf{x}_{ai}, \omega) \cos(\omega t + \varphi_P(\mathbf{x}_{ai}, \omega)) \tag{31}$$

where, considering Eq. (30), $P(\mathbf{x}_{ai}, \omega) = |p(\mathbf{x}_{ai}, \omega)| = |j\omega Z_{ij}(\omega) \alpha_{rj}(\omega) f_r(\mathbf{x}_{cf}, \omega)|$ and $\varphi_P(\mathbf{x}_{ai}, \omega) = \angle\{p(\mathbf{x}_{ai}, \omega)\} = \angle\{j\omega Z_{ij}(\omega) \alpha_{rj}(\omega) f_r(\mathbf{x}_{cf}, \omega)\}$ are respectively the amplitude and phase of the sound pressure at each point where the sound field is depicted. Here, the operational acoustic shapes were derived from Eq. (31) with respect to the same instant of time of maximum amplitude of the flexural vibration fields, that is when $|\cos(\omega t + \varphi_U(\mathbf{x}_{ci}, \omega))| = 1$. Equations (30) and (31) indicate that, for time-harmonic vibrations, the amplitude of the acoustic pressure at a given instant of time is modulated by the structural response of the thin-walled cylinder, i.e. via the dynamic flexibility $\alpha_{rj}(\omega)$, and by the acoustic response generated by the radiation of the baffled cylinder, i.e. via the acoustic impedance $Z_{ij}(\omega)$. To conclude it is noted that in case the laser vibrometer measurements were employed to generate the acoustic field, then the formulation presented in this section was employed setting

$$j\omega \alpha_{rj}(\omega) = Y_{rj}(\omega) \tag{32}$$

where $Y_{rj}(\omega)$ are the mobility functions measured by the laser vibrometer as defined in Eq. (15).

4. Measurement results

The methodology proposed above to reconstruct the cylinder flexural vibration and sound radiation fields is now assessed for camera measurements taken with the experimental apparatus presented in Section 2.2 and shown in Fig. 2a. The vibration maps reconstructed from the camera measurements are validated on a qualitative level with respect to vibration maps obtained from the laser vibrometer measurements taken with the setup described in Section 2.3 and Fig. 3a. Also, the acoustic maps derived from the camera measurements are validated on a qualitative level with those calculated from the laser vibration measurements and with those obtained directly from acoustic measurements taken with the setups described in Section 2.3 and Fig. 3b,c.

Before moving into the analysis of the reconstructed flexural vibration and sound radiation maps, to provide a background understanding of the flexural response and sound radiation of the cylinder, the two quantities are first analysed in the frequency domain

with respect to the spectrum of the spatially averaged flexural vibration per unit force excitation and the spectrum of the sound pressure per unit force excitation at a given monitor point $\mathbf{x}_{am} = (r'_m, \theta'_m, z'_m)$ of coordinates $r'_m = 219\text{mm}, \theta'_m = 0deg, z'_m = 0\text{mm}$. Then the comparative analysis between the maps of the cylinder flexural vibration and sound radiation obtained from the camera measurements and from the laser and microphones measurements are presented and analysed.

4.1. Spectra of the spatially averaged flexural vibration and sound pressure at a monitor point per unit force excitation

The global flexural response of the thin-walled cylinder is assessed with respect to the time-averaged total flexural kinetic energy, which is given by the following expression:

$$\overline{K} = \lim_{T\to\infty} \frac{1}{T} \int_0^T \int_{S_c} \frac{1}{2} \rho_c h v_r(\mathbf{x}_c, t)^2 dS_c dt \tag{33}$$

where, according to Eq. (16) $v_r(\mathbf{x}_c, t)$ is the radial velocity of the cylinder at position $\mathbf{x}_{cj} = (R, \theta, z)$, ρ_c is the density of the cylinder material and h, S_c are the thickness and lateral area of the cylinder. For time harmonic vibrations, this equation becomes

$$\overline{K}(\omega) = \frac{\rho_c h}{4} \int_{S_c} |v_r(\mathbf{x}_c, \omega)|^2 dS_c \tag{34}$$

where $v_r(\mathbf{x}_{cj}, \omega)$ is the complex amplitude of the radial velocity at position $\mathbf{x}_c$. Considering the dynamic flexibility FRFs measured with the camera setup

$$\overline{K}(\omega) \approx \frac{\omega^2 M_c}{4N_e} \sum_{j=1}^{N_e} |\alpha_{rj}(\omega)|^2 |f_r(\mathbf{x}_{cf}, \omega)|^2 \tag{35}$$

whereas considering the mobility FRFs measured with the laser vibrometer

$$\overline{K}(\omega) \approx \frac{M_c}{4N_e} \sum_{j=1}^{N_e} |Y_{rj}(\omega)|^2 |f_r(\mathbf{x}_{cf}, \omega)|^2 \tag{36}$$

Here M_c is the mass of the cylinder, N_e is the number of quadrangular elements.

To start with, Fig. 5 shows the spectrum of the time-averaged total flexural kinetic energy per unit force excitation derived with Eq. (36) from the laser vibrometer measurements in a frequency range comprised between 500 and 1500 Hz. The figure encompasses small pictures with the deflection shapes at the resonance frequencies. In general, the spectrum is characterised by distinct resonance peaks, which suggests that in the 500 – 1500 Hz range the flexural response is characterised by a low modal overlap [50]. Indeed, apart from few cases, the deflection shapes at the resonance frequencies show the typical regular pattern for the flexural natural modes of a

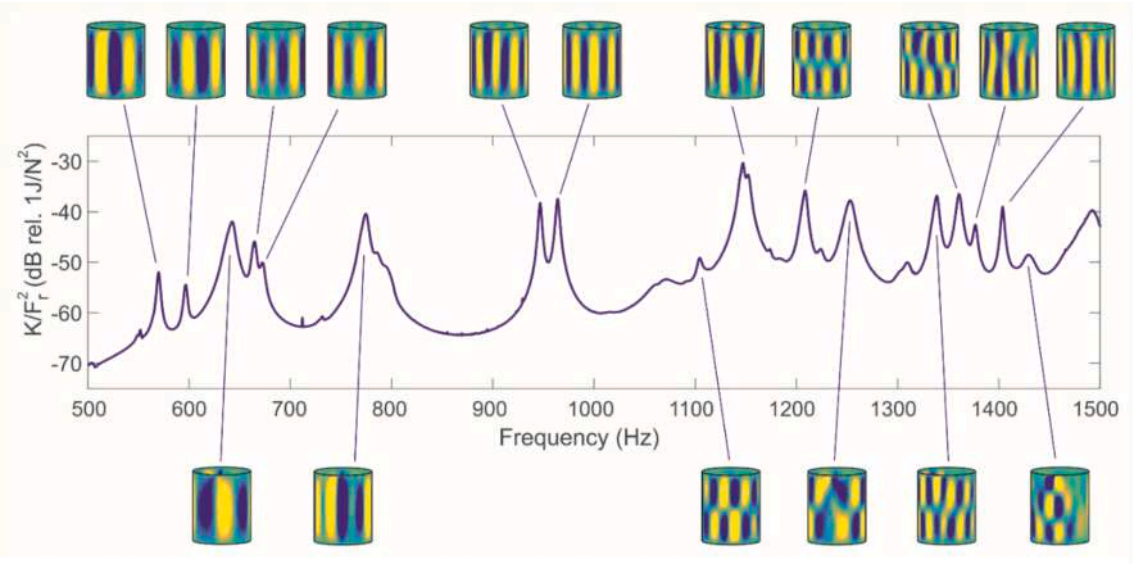

Fig. 5. Spectrum of the total flexural kinetic energy per unit force excitation derived from laser vibrometer measurements with the deflection shapes at the resonance frequencies.

clamped cylinder (e.g. see Refs. [60–63]). In general, the deflection shapes show quite high circumferential mode orders that span from 5 to 11 and rather low axial mode orders equal to 1 or 2. In the latter case, as can be noticed in Fig. 5, the mode shapes are characterised by a circumferential nodal line exactly in the middle span of the cylinder height. There is just a deflection shape at about 1440 Hz, which shows a mode order 3 in axial direction.

Moving to the flexural vibrations reconstructed from the camera measurements, the red line in Fig. 6 shows the spectrum of the time-averaged total flexural kinetic energy per unit force excitation derived with the formulation presented in Sections 2.1 and 2.2 and then calculated with Eq. (35) in the 500 – 1500 Hz frequency range. To allow a direct comparison, the spectrum obtained from the laser vibration measurements is reported as well with the blue line. The two spectra overlap quite well. There are small shifts of few resonance frequencies and also small mismatches of the amplitudes of the resonance peaks. These small gaps are most likely due to the fact that the measurements had not been taken simultaneously. Moreover, the measurement taken with the laser vibrometer took several hours such that the response of the clamped cylinder was affected by a significant variability induced by ambient temperature changes and heating effects produced by the shaker located inside the cylinder. The spectrum obtained from the camera measurements is slightly noisier that that derived from the laser vibrometer measurements, particularly at the higher frequency end of the measurement range. Nevertheless, the two measurements show quite a remarkable global agreement, which is confirmed also by the deflection shapes reported in the two figures for the vibrometer and camera measurements respectively. The deflection shapes at higher resonance frequencies depicted in Fig. 6 show a comparatively more irregular shape than those plotted in Fig. 5. This indicates that indeed, the results obtained from the camera measurements are slightly less accurate than those obtained from the laser vibration measurements, although as will be shown below, and can already be seen in the spectral analysis, they have little impact on the overall vibration and thus on the sound radiation.

The sound radiation is instead assessed at the monitor position $r'_m = 219\text{mm}, \theta'_m = 0deg, z'_m = 0\text{mm}$ with respect to the time-averaged sound pressure per unit force excitation either measured with a microphone (black lines in Fig. 7) or derived from Eq. (30) using the vibration FRFs acquired with the laser vibrometer (blue line in Fig. 7a) or reconstructed from the camera measurements (red line in Fig. 7b). Comparing first the spectrum of the sound pressure measured with the microphone with the spectrum in Fig. 5 for the spatially averaged vibration measured with laser vibrometer it is noted that the two spectra show similar features, although the resonance peaks in the acoustic spectrum have quite an uneven range of amplitudes and there are some antiresonance troughs in between resonances. This is the result of the fact that, at each frequency, the amplitude of the acoustic field is modulated by the radiation efficiency of the cylinder flexural modes that mainly contribute to the response at that frequency [28]. Therefore, the sound pressure at certain resonance frequencies, where the response is controlled by the resonant mode [28,50], may result significantly attenuated when the resonant mode has a low radiation efficiency. Moreover, the acoustic spectrum provides the sound pressure at a point where, as it will be shown in the forthcoming section, at certain frequencies the sound field may be characterised by destructive interference effect that lessen significantly the sound pressure. The plots in Fig. 7 show that, in general, the spectra of the sound pressure derived from the laser vibrometer (blue line in Fig. 7a) or the camera (red line in Fig. 7b) measurements reproduce rather well the principal features of the spectrum measured directly with the microphone. There are some marked differences over small frequency bandwidths, whose nature is difficult to identify. In fact, the spectra based on direct measurements of the sound pressure may have been affected by small noise (e.g. the acquisition system that was kept in the measurement room) and flanking sources (e.g. structure-

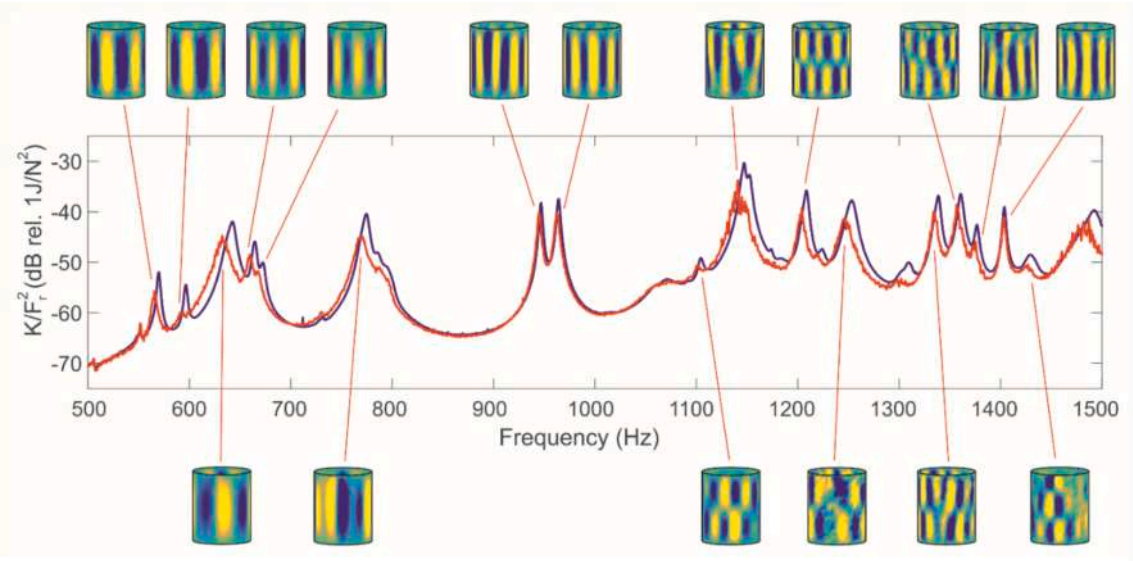

Fig. 6. Spectrum of the total flexural kinetic energy per unit force excitation derived from camera measurements (red line) with the deflection shapes at the resonance frequencies (compared with laser vibrometer measurements, blue line). (For interpretation of the references to colour in this figure legend, the reader is referred to the web version of this article.)

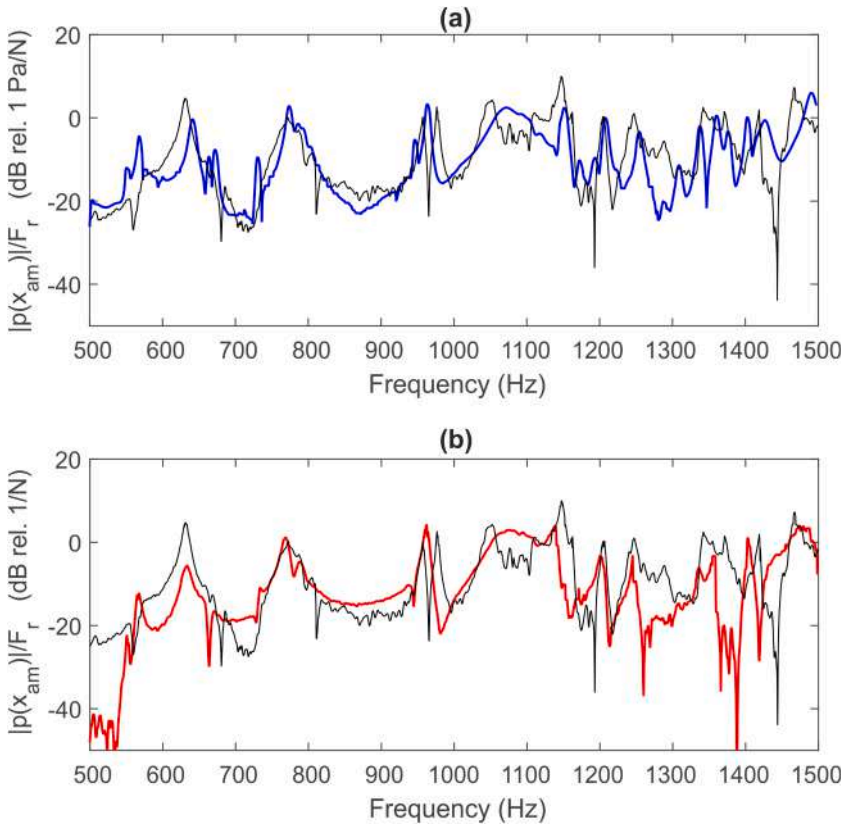

Fig. 7. Spectra of the sound pressure at a monitor point per unit force excitation derived from microphone measurement (black lines), laser vibrometer measurements (blue line) and camera measurements (red line). (For interpretation of the references to colour in this figure legend, the reader is referred to the web version of this article.)

borne noise due to vibrations transmitted from the cylinder to the floor of the anechoic room). Instead, the spectrum derived from the laser vibrometer measurements may have been affected by the variability of the flexural response of the cylinder during the long-lasting measurements (several hours). Finally, the spectrum derived from the camera measurements may have been limited by the spatial resolution of the camera employed in this work. Rather importantly, the three set of measurements couldn't be taken simultaneously and thus the response of the structure may have changed from one measurement to another. Nevertheless, the spectra shown in Fig. 7a,b indicate that the proposed approach based on the reconstruction of the sound radiation using a discretized version of the Kirchhoff-Helmholtz integral and the vibration field reconstructed from multi-view measurements taken with an optical camera can be successfully employed to derive the sound radiation from a closed shell over a wide audio frequency range.

4.2. *Flexural vibration and sound radiation fields from camera and laser-microphones measurements*

This section presents the maps of the flexural vibration and sound radiation fields of the baffled cylinder model structure reconstructed from multi-view camera acquisitions taken with the setup shown in Fig. 2 and measured with the laser vibrometer shown in Fig. 3a and the microphones array shown in Fig. 3b,c. The vibration and sound radiation fields have been reconstructed and measured for time-harmonic force excitations at four resonance frequencies; that is at $f_1 = 618$ Hz, $f_2 = 659$ Hz, $f_3 = 964$ Hz and $f_4 = 1231$ Hz. As can be noticed in Figs. 5 and 6, apart from few resonances, the spectrum of the cylinder flexural vibration shows sharp peaks, which suggests that, in the 500 – 1500 Hz frequency range, the flexural vibration is characterised by a low modal overlap [50] such that, at most resonance frequencies, the response is controlled by the resonant mode only as, indeed, one can notice in the small views of the deflection shapes reported on the graphs themselves. Accordingly, it is expected that the radiated sound field near the cylinder surface should be characterised by a circle of acoustic lobes that comply with the circumferential lobes of the resonating flexural mode. The reconstructed and measured acoustic fields are depicted in Figs. 8 – 11. More specifically, the maps (a) show the vibration and acoustic fields reconstructed from camera measurements. The maps (b) show the vibration and acoustic fields obtained directly from, and reconstructed from, the laser vibrometer measurements. Finally, the maps (c) show the fields obtained from direct measurements with the laser vibrometer and the microphones array respectively.

Fig. 8 shows that the time-harmonic vibration field at $f_1 = 618$ Hz is characterised by the natural flexural mode with axial mode order $n_z = 1$ and circumferential mode order $n_\theta = 5$. The field reconstructed from the camera measurement depicted in (a) closely

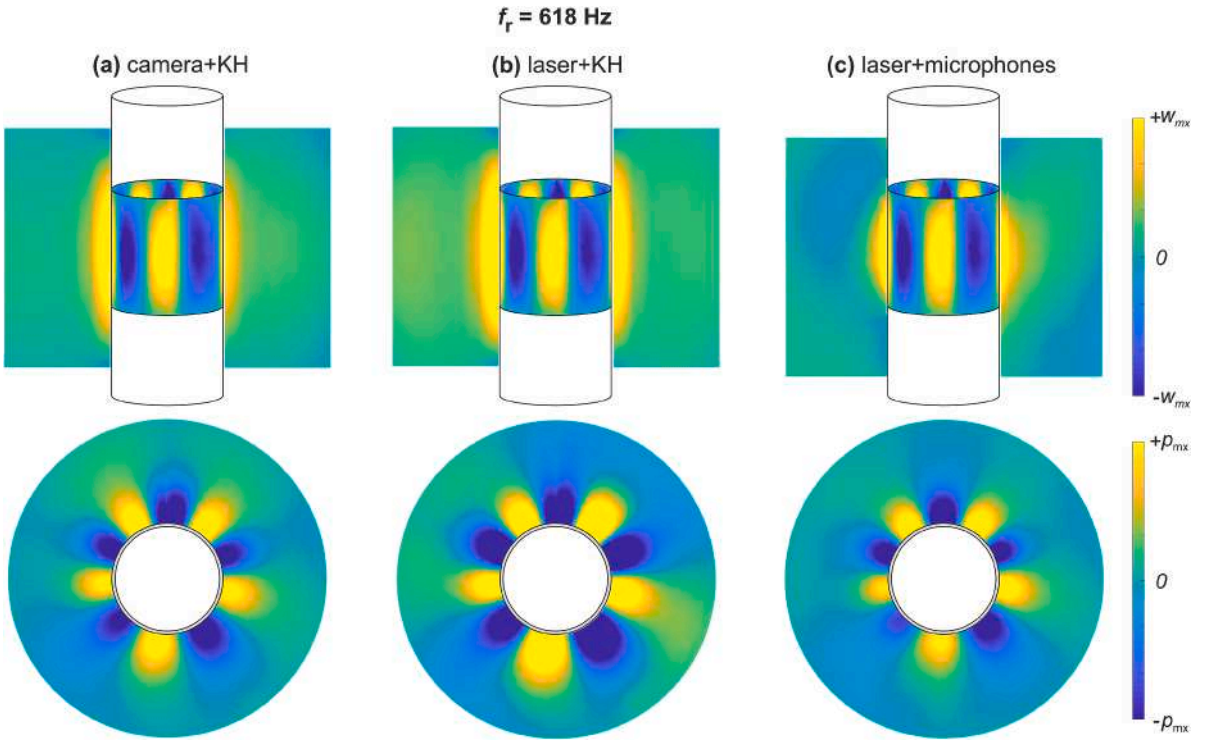

Fig. 8. Vibration and sound radiation fields reconstructed from (a) camera measurements and KH simulation, (b) laser-vib. measurements and KH simulation, (c) laser-vib. measurements and microphones-array measurements at the resonance frequency fr = 618 Hz.

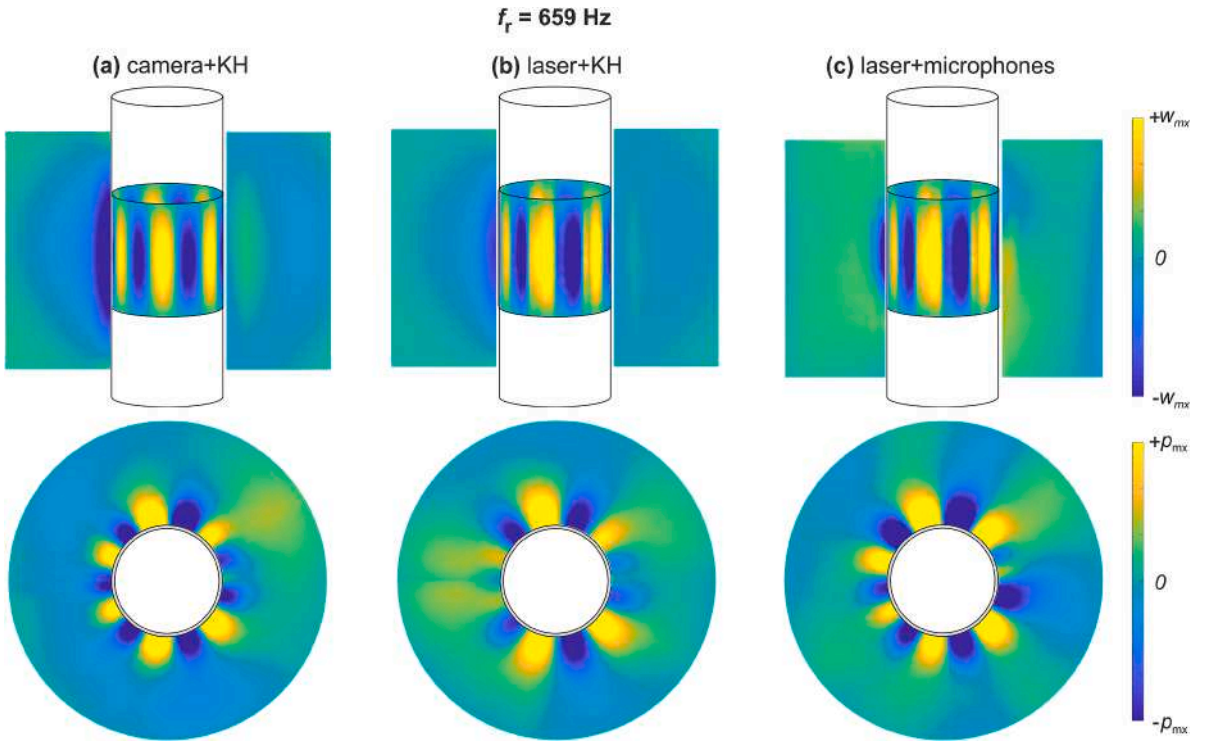

Fig. 9. Vibration and sound radiation fields reconstructed from (a) camera measurements and KH simulation, (b) laser-vib. measurements and KH simulation, (c) laser-vib. measurements and microphones-array measurements at the resonance frequency fr = 659 Hz.

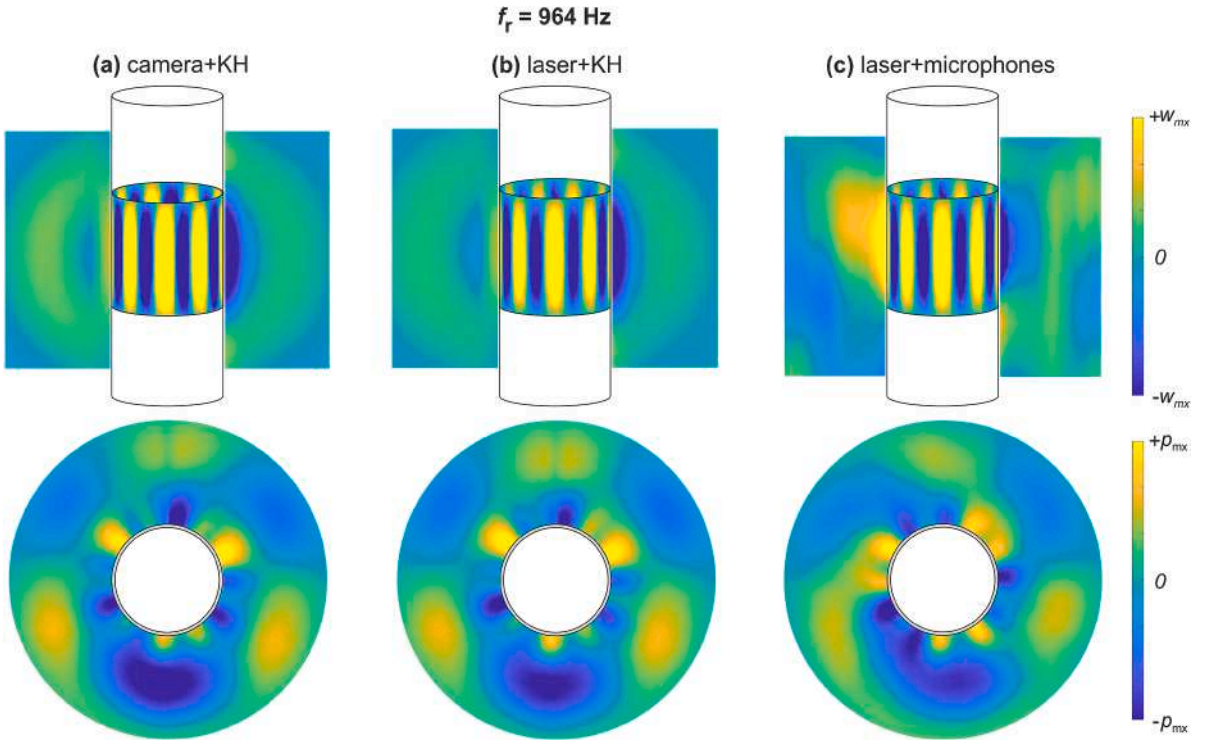

Fig. 10. Vibration and sound radiation fields reconstructed from (a) camera measurements and KH simulation, (b) laser-vib. measurements and KH simulation, (c) laser-vib. measurements and microphones-array measurements at the resonance frequency fr = 964 Hz.

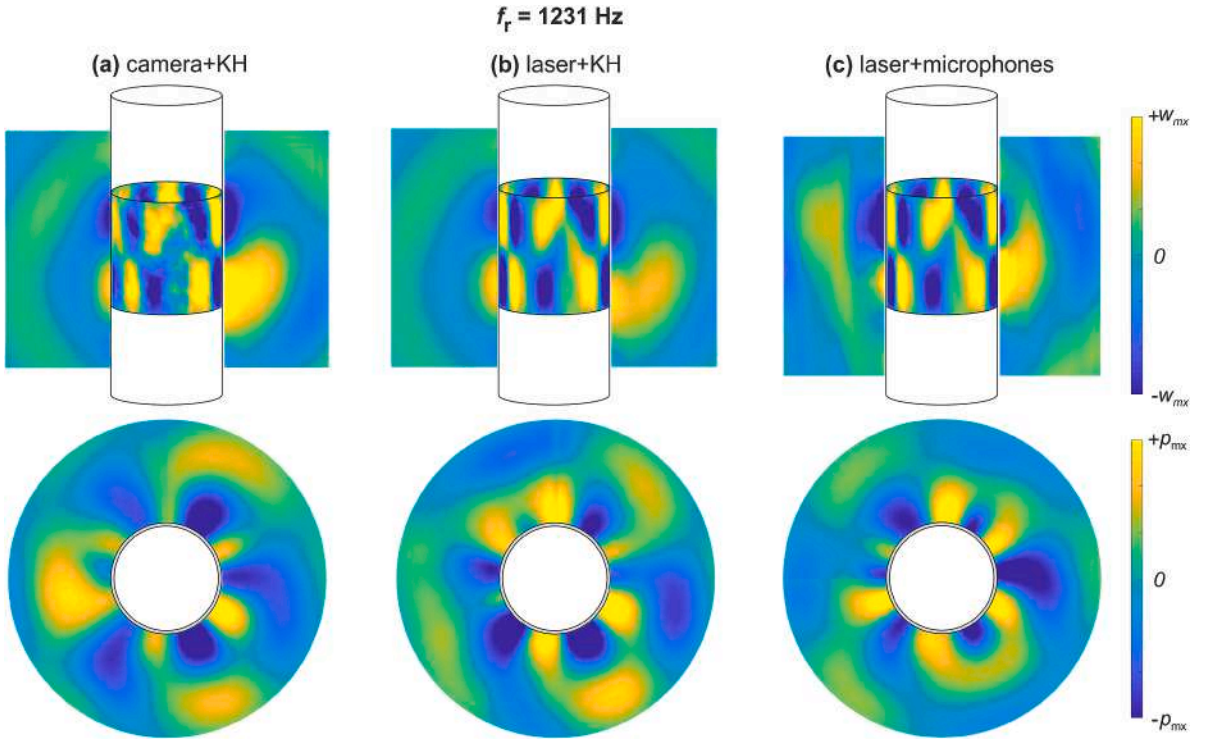

Fig. 11. Vibration and sound radiation fields reconstructed from (a) camera measurements and KH simulation, (b) laser-vib. measurements and KH simulation, (c) laser-vib. measurements and microphones-array measurements at the resonance frequency fr = 1231 Hz.

overlaps with that measured with the laser vibrometer shown in (b) and (c). The magnitude of the field derived from the laser vibrometer measurements is slightly bigger than that obtained from the camera measurements. This mismatch is however marginal and possibly due to the fact that the two measurements could not be taken simultaneously, primarily because the camera acquisitions took much less time than the measurements with the laser vibrometer. The acoustic map in (a) obtained from the camera measurements shows that, in the vicinity of the cylinder, the radiated acoustic field in the horizontal midplane is characterised by 10 lobes, which closely replicates the wavy shape of the flexural mode in circumferential direction. The same effect is seen in the vertical plane where the acoustic field is characterised by a single lobe that matches the vibration field in vertical direction. The acoustic field (a) reconstructed from the camera measurements agrees quite well both with that reconstructed from the laser vibrometer measurements shown in (b) and with that measured directly with the microphones array depicted in (c). The nearfield lobes in (b) extend over a slightly bigger area, but this may be the result of the small mismatch in the amplitude of the camera and laser vibrometer vibration fields discussed above. Instead, the lobes in (c) extend over a slightly smaller surface, and this could be the result of the approximations introduced by the measurement setup. In general, the small differences between the reconstructed and measured vibration and sound fields could be simply due to the fact that the measurements cannot be taken simultaneously and thus the response of the cylinder as well as the excitation generated by the shaker may have changed a little from measurement to measurement.

Moving to the time-harmonic excitation at $f_2 = 659$ Hz, Fig. 9, shows that the vibration field is controlled by the natural flexural mode with axial mode order $n_z = 1$ and circumferential mode order $n_\theta = 7$. Here too, contrasting the three vibration maps, the field reconstructed from the camera measurement in (a) overlaps quite well with that measured with the laser vibrometer in (b) and (c). The acoustic nearfield reconstructed from the camera measurements shown in (a) is characterised 14 lobes with alternating positive–-negative sound pressure in the horizontal mid plane and a single lobe in the vertical plane, which copy the wavy shape of the flexural mode in circumferential and axial directions. The acoustic field (a) reconstructed from the camera measurements agrees rather well with that measured directly with the microphones array depicted in (c) apart from small mismatches, which, in this case too, are likely to be due to the fact that the two sets of measurements could not be taken simultaneously. Also, the acoustic field (a) closely replicates that reconstructed from laser vibrometer measurements shown in (b) apart from the lobes on the left-hand side, which, however, were not properly reconstructed from the laser vibration measurements that presented small errors in that area.

Considering now Fig. 10, the vibration measurements show that the time-harmonic vibration field at $f_3 = 964$ Hz is controlled by the natural flexural mode with axial mode order $n_z = 1$ and circumferential mode order $n_\theta = 9$. Again, the field in (a) obtained from the cameras measurements agrees well with that in (b) and (c) measured directly with the laser vibrometer. Here, the shape of the radiated acoustic field is somewhat more complex than that found at the first two resonance frequencies. Once more, the field in the horizontal plane presents a ring of lobes with alternating positive–negative sound pressure that somehow replicates the wavy vibration field in circumferential direction of the cylinder. However, in this case, there is also a second ring formed by a total of 6 bigger lobes, yet with alternating positive–negative sound pressures. These features are found too in the acoustic fields reconstructed from the laser vibrometer measurements and in those measured directly with the array of microphones. Here, the shape and the intensity of the small lobes adjacent to the cylinder are not the same for all lobes. This is probably the result of two concurrent effects. On the one hand the vibration field with high circumferential mode order generates these smaller lobes, whose shape and intensity can be affected primarily by small errors in the measurements. Also, the longitudinal welding of the cylinder wall may have had a bigger impact on the sound radiation. These features reflect quite significantly on the lobe in the vertical plane too. In fact, the small deviations in circumferential directions of the nearfield lobes, generate quite significant differences in the sound fields depicted in the vertical planes. This mismatch could be due to the fact that the acoustic measurements on the vertical plane were taken with a small angular offset too. Overall, the results presented in Fig. 10 confirm a good agreement of the vibration and sound radiation fields reconstructed from the camera measurements with both those obtained from the laser vibrometer measurements and those measured directly with the laser vibrometer and microphone array.

To conclude, the maps depicted in Fig. 11 for the flexural vibration and sound radiation at $f_4 = 1231$ Hz are analysed here. As can be seen in the top pictures, in this case the flexural vibration field is characterised by a flexural mode with axial mode order $n_z = 2$ and circumferential mode order $n_\theta = 6$. Hence, the vibration field is cut in two sections along the length, with a circular nodal line at the middle span, which divides the alternating vibration lobes in two rings having an angular offset such that the $n_z = 2$ positive and negative vibration lobes develop along the length. Here the vibration field (a) reconstructed from the camera measurements is slightly irregular, although, overall, it reproduces the shape obtained from the measurement taken with the laser vibrometer (b) and (c). This is likely to be caused by the fact that, as can be noticed in the spectrum plotted in Fig. 6, the measurements are close to the upper limit of the frequency range that can be handled by the camera. Nevertheless, as can be seen in the map (a), the sound field reconstructed from the camera acquisitions, is quite smooth and, in fact, it replicates reasonably well both that reconstructed from the laser vibrometer measurement in (b) and that measured directly with the arrays of microphones in (c). Here again the acoustic field is characterised by two rings of lobes having alternated positive–negative sound pressures. The inner ring of lobes conforms to the wavy flexural vibration with circumferential mode order $n_\theta = 6$. The sound field in the vertical plane reconstructed from the camera acquisitions (a) shows the two positive–negative sound pressure lobes that conform to the vibration field in axial direction. The field replicates quite well that generated from the vibration measurements taken with the vibrometer as well as that measured directly with the microphones. Overall, despite the vibration field reconstructed from the camera measurements showed quite an irregular shape, the resulting acoustic field calculated with the approximated Kirchhoff-Helmholtz formulation is rather smooth and, also, agrees reasonably well with those either reconstructed from the laser vibrometer measurements or measured directly with the microphones array. This phenomenon was noticed and examined in Ref. [34] too, which demonstrated how the irregular vibration field is actually characterised by a random distribution of small errors due to the digitalization of the images in the camera. Nevertheless, since the sound pressure at each point of the free field results from the radiation generated by the whole surface of the cylinder, the effects of these

errors are cumulated in such a way as they cancel out and thus a rather accurate map of the sound radiation is produced.

To conclude, the accuracy of the reconstructed vibration and sound fields have been quantified considering the differences in dB (thus ratios in linear terms) between the sum of the reconstructed and measured modulus-squared vibration velocities and between the sum of the reconstructed and measured modulus-squared sound pressures using the following formulae:

$$\Delta v_{r,cv}(\omega_r) = 10log_{10}\frac{\sum_j \left|v_{r,c}\left(\mathbf{x}_{cj},\omega_r\right)\right|^2}{\sum_j \left|v_{r,v}\left(\mathbf{x}_{cj},\omega_r\right)\right|^2} \tag{37}$$

$$\Delta p_{cm}(\omega_r) = 10log_{10}\frac{\sum_i |p_c(\mathbf{x}_{ai},\omega_r)|^2}{\sum_i |p_m(\mathbf{x}_{ai},\omega_r)|^2} \tag{38}$$

$$\Delta p_{vm}(\omega_r) = 10log_{10}\frac{\sum_i |p_v(\mathbf{x}_{ai},\omega_r)|^2}{\sum_i |p_m(\mathbf{x}_{ai},\omega_r)|^2} \tag{39}$$

$$\Delta p_{cv}(\omega_r) = 10log_{10}\frac{\sum_i |p_c(\mathbf{x}_{ai},\omega_r)|^2}{\sum_i |p_v(\mathbf{x}_{ai},\omega_r)|^2} \tag{40}$$

here $v_{r,c}\left(\mathbf{x}_{cj},\omega_r\right)$ and $v_{r,v}\left(\mathbf{x}_{cj},\omega_r\right)$ are the complex radial velocities at the j-*th* point of the vibration grid depicted in Fig. 1b reconstructed from the camera measurements and measured with the laser vibrometer respectively. Also, $p_c(\mathbf{x}_{ai},\omega_r)$, $p_m(\mathbf{x}_{ai},\omega_r)$ and $p_v(\mathbf{x}_{ai},\omega_r)$ are the complex sound pressures at the the i-*th* point of the acoustic grids depicted in Fig. 1b,c reconstructed from the camera and from the laser vibrometer measurements and measured with the array of microphones. The results summarised in Table 1 show that, on average, the vibration field reconstructed from the camera acquisitions deviates by 0.7 to 3.2 dB from that measured with the laser vibrometer. The differences are all positive, which suggests there could have been a systematic error, possibly due to the fact that the two measurements were taken not simultaneously and, actually, the laser vibration measurement lasted few hours compared to the few tents of minutes necessary for the camera acquisitions. Nevertheless the 0.7 to 3.2 dB errors confirm the potentials of vibration measurements with optical cameras at higher audio frequencies too. Moving to the sound radiation errors, the data in Table 1 indicate that, on average, the sound field reconstructed from the camera acquisitions deviates by 0.4 to 2.0 dB from that measured with the microphones array and by 0.6 to 4.0 dB from that reconstructed from laser vibrometer measurements. Overall, there are some differences between the two sets of errors, which are confirmed by the 0.2 to 4.2 dB differences between the sound field reconstructed from the laser vibrometer measurements and measured directly with the microphones array. There is no a clear correlation between the three sets of errors, which, yet again, may be the result of the fact that the three sets of measurements could not be implemented simultaneously and more importantly lasted for significantly different amount of time. Overall, the 0.4 to 2.0 dB errors found between the fields reconstructed with the cameras and those measured directly with the microphone array suggest that the proposed methodology to measure sound radiation with optical cameras can be a viable practical solution.

5. Conclusions

This paper has introduced a method for the measurement and reconstruction of 3D sound radiation of a closed shell structure using a single high-speed optical camera. The study has presented measurements of the flexural vibration and sound radiation fields taken on a baffled thin-walled cylinder model structure, which have been validated against vibration and acoustic measurements taken with a scanner laser vibrometer and a microphone array. The results of the measurement campaigns suggest that optical cameras can be suitably used to detect and reconstruct the sound radiation fields of closed shells. Overall, considering the four resonance frequencies analysed in the study, on average, the vibration field reconstructed from the camera acquisitions deviates by 0.7 to 3.2 dB from that measured with the laser vibrometer. Also, the acoustic field reconstructed from the camera acquisitions deviates by 0.4 to 2.0 dB from that measured with the microphones array. The proposed method enhances and simplifies the measurement and reconstruction processes in quite a few aspects, which are detailed below.

Table 1
Differences of the spatially averaged cylinder radial velocities estimated from the camera measurements and measured with the laser vibrometer and differences of the spatially averaged radiated sound pressure reconstructed from camera measurements and laser vibrometer measurements and measured with microphones at the four reference resonance frequencies.

Resonance Frequency (Hz)	Cylinder $\Delta\dot{w}$ (dB)	Vertical Plane Δp (dB)			Horizontal Plane Δp (dB)		
	Δv_{cv}	Δp_{cm}	Δp_{cv}	Δp_{vm}	Δp_{cm}	Δp_{cv}	Δp_{vm}
618	+0.7	−2.0	+0.1	−2.0	−2.5	−0.6	−1.9
659	+2.1	−1.9	+1.0	−2.9	−1.8	+1.3	−3.2
964	+3.2	+0.4	+4.6	−4.2	+0.4	+4.4	−4.1
1231	+2.7	+1.2	+2.0	−0.8	+1.0	+1.2	−0.2

1) The proposed approach can be suitably implemented in situ without the need of moving the tested equipment or structure into acoustic facilities such as large reverberant or anechoic rooms.
2) The optical camera measurement setup does not influence neither the vibration response nor the sound radiation of the tested equipment or structure.
3) With sufficiently large and dampened measurement environments, the sound reflected by the outer walls and the presence of flanking sources and background noise have negligible effect on the reconstruction of the sound field radiated by the tested equipment or structure.
4) The full-field camera acquisition allows for accurate identifications of both the whole flexural vibration field and the whole sound ration field at rather dense grids of points.
5) The actual camera recordings are rather fast and can be completed in few minutes such that the measurement is not affected by variability of the structural response or other exogenous disturbances that may arise during long lasting experimental tests.
6) The camera acquisitions can be employed to reconstruct the actual geometry of equipment or structures with complex shape, in which case the sound radiation should be derived with Boundary Element Method and Finite element Method numerical approaches.

The proposed method is characterised by some important limitations too, which can be summarised in the following three points.

1) The vibration field is reconstructed in terms of displacements, whose amplitude is bound to be much smaller than velocities or accelerations, particularly at higher frequencies.
2) The data postprocessing is rather cumbersome and requires rather powerful computing equipment for the derivation of both the vibration and acoustic fields.
3) A speckled pattern should be bonded or painted on the radiating surfaces of the tested object such that the specific vibration points can be identified on the camera recordings, for example with DIC.

It is expected that these limitations can be lifted to some extent both by further research on the optical measurement technique and on the data post processing to generate the flexural vibration and sound radiation fields and by the development of higher speed and higher resolution cameras such that the positive features listed above can be fully exploited. In general, the measurement technique can prove be useful in practical applications where there is an interest into the identification of the whole radiation field. Also, it can be employed to detect the spectrum of the total sound power radiation by partitions or machinery housed in closed shells.

CRediT authorship contribution statement

Sofia Baldini: Writing – review & editing, Writing – original draft, Visualization, Validation, Methodology, Investigation, Data curation, Conceptualization. **Gianluca Guernieri:** Writing – review & editing, Writing – original draft, Visualization, Validation, Methodology, Investigation, Data curation, Conceptualization. **Domen Gorjup:** Writing – review & editing, Writing – original draft, Visualization, Validation, Methodology, Investigation, Data curation, Conceptualization. **Paolo Gardonio:** Writing – review & editing, Writing – original draft, Visualization, Validation, Methodology, Investigation, Data curation, Conceptualization. **Janko Slavič:** Writing – review & editing, Writing – original draft, Visualization, Validation, Methodology, Investigation, Data curation, Conceptualization. **Roberto Rinaldo:** Writing – review & editing, Writing – original draft, Visualization, Validation, Methodology, Investigation, Data curation, Conceptualization.

Declaration of competing interest

The authors declare that they have no known competing financial interests or personal relationships that could have appeared to influence the work reported in this paper.

Acknowledgements

The authors would like to acknowledge the ESPERT project which was supported by the University of Udine Research Programme and the partial financial support from the Slovenian Research Agency, Slovenia (research core funding No. P2-0263).

Appendix A. . MatLab code for the derivation of the sound radiation field

This appendix reports the MatLab codes used to derive the sound radiation field from the flexural vibration of the cylinder measured with optical methods as discussed in Section 2.

```
function p=acoust_press(r,theta,z, a, sourcethetaz, sourcev, f0, c0, rho0, S,
   M, tol, Madd)
% Computes the contribution of all source elements
% to the target at r,theta,z.
```

(*continued on next page*)

(*continued*)

```
% r,theta,z, coordinates of the target point
% a cylinder radius
% sourcethetaz Ne x 2 matrix with the theta, z coordinates of the source
% elements on the cylinder
% sourcev Ne x 1 vector with the velocities of the source points in sourcethetaz
% f0 frequency
% c0 speed of sound
% rho0 density of medium
% S area element
% M number of ponts between 0 and k (default M=180)
% tol tolerance to stop integration (default tol=1e-4)
% Madd additional terms for kz beyond k - imaginary argument (default Madd=1000)
if nargin==10
M=180;
tol=1e-4;
Madd=1000;
end
Ne=size(sourcethetaz,1);
p=0;
for i=1:Ne
thetas=sourcethetaz(i,1);
zz=sourcethetaz(i,2);
v=sourcev(i);
p=p+zij(r,theta,z, a, thetas, zz, f0, c0, rho0, S, v, M, tol, Madd);
end
function p=zij(r,theta,z, a, thetas, zz, f0, c0, rho0, S, v, M, tol, Madd)
% Computes the contribution of a single source element
% at a, thetas, zz to the target at r,theta,z
% r,theta,z, coordinates of the target point
% a, thetas, zz coordinates of source point, with a cylinder radius
% f0 frequency
% c0 speed of sound
% rho0
% S area element
% v velocity of source element
% M number of integration points between 0 and k (default M=180)
% tol tolerance to stop integration (default tol=1e-4)
% Madd additional terms for kz beyond k - imaginay argument (default Madd=1000)
if nargin==11
M=180;
tol=1e-4;
Madd=1000;
end
omega=2*pi*f0;
k=omega/c0;
delta=k/M;
p=-1i*rho0*omega*S*v*delta/(2*pi^2);
small_disp=delta/20;
n=0;
kz=(0:M+Madd-1)*delta+small_disp;
arg1=(sqrt(k^2-kz.^2)*a);
arg2=(sqrt(k^2-kz.^2)*r);
idxr=find(real(arg1)~=0);
idxi=find(real(arg1)==0);
add=sum((cos(kz(idxr)*(z-zz)).*besselh(n,2,arg2(idxr))./...
(arg1(idxr).*dbesselh(n, 2, arg1(idxr))));
add=add+sum((cos(kz(idxi)*(z-zz)).*besselk(n,abs(arg2(idxi)))./...
(abs(arg1(idxi)).*dbesselk(n, abs(arg1(idxi)))));
en=2;
while (1)
n=n+1;
addi=en*cos(n*(theta-thetas))*sum((cos(kz(idxr)*(z-zz)).*besselh(n,2,arg2
    (idxr))./...
(arg1(idxr).*dbesselh(n, 2, arg1(idxr))));
addi=addi+ en*cos(n*(theta-thetas))...
*sum((cos(kz(idxi)*(zz)).*besselk(n,abs(arg2(idxi)))./...
(abs(arg1(idxi)).*dbesselk(n, abs(arg1(idxi)))));
add=add+addi;
if ((abs((addi))<tol*abs(add)) || (n>50)) % limit sum to n=50
break;
end
```

(*continued on next page*)

(*continued*)

```
end
p=p*add;
function y=dbesselh(n,type,z)
% Computes the derivative of the Hankel function.
y=0.5*(besselh(n-1,type,z) - besselh(n+1,type,z));
function y=dbesselk(n,z)
% Computes the derivative of the modified Bessel function of the second kind
y=-0.5*(besselk(n-1,z) + besselk(n+1,z));
```

Data availability

Data will be made available on request.

References

[1] R.F. Barron, Industrial Noise Control and Acoustics, Dekker, 2003.
[2] D.A. Bies, C.H. Hansen, Engineering Noise Control: Theory and Practice, CRC Press, 2017.
[3] B. Cuyx, W. Desmet, W. Buyens, T. van Waterschoot, Design and validation of a low-cost acoustic anechoic chamber, J. Audio Eng. Soc. 149 (2020) 1–5.
[4] D. Habault, E. Friot, P. Herzog, C. Pinhede, Active control in an anechoic room: theory and first simulations, Acta Acust. Acust. 103 (2017) 369–378, https://doi.org/10.3813/aaa.919066.
[5] C. Pinhède, D. Habault, E. Friot, Ph. Herzog, Active control of the field scattered by the rigid wall of a semi-anechoic room—Simulations and full-scale off-line experiment, J. Sound Vib. 506 (2021) 116134, https://doi.org/10.1016/j.jsv.2021.116134.
[6] C. Pinhède, R. Boulandet, E. Friot, M. Allado, R. Côte, P. Herzog, Towards an active semi-anechoic room : simulations and first measurements, in: Proceedings of the 10th Convention of the European Acoustics Association Forum Acusticum 2023, European Acoustics Association, Turin, Italy, 2022: pp. 3611–3618. https://doi.org/10.61782/fa.2023.0399.
[7] R. Haasjes, A.P. Berkhoff, An efficient offline scheme to compute an FIR controller for active reduction of acoustic reflections in an anechoic chamber, J. Sound Vib. 573 (2024) 118198, https://doi.org/10.1016/j.jsv.2023.118198.
[8] F. Fahy, Sound Intensity, second ed., E & FN Spon, 1995.
[9] F. Jacobsen, H.-E. de Bree, A comparison of two different sound intensity measurement principles, J. Acoust. Soc. Am. 118 (2005) 1510–1517, https://doi.org/10.1121/1.1984860.
[10] X. Yang, G. Zhu, Y. Miao, Calibration of sound intensity instruments based on the double coupler technology, Appl. Acoust. 199 (2022) 109008, https://doi.org/10.1016/j.apacoust.2022.109008.
[11] D.F. Comesaña, S. Steltenpool, M. Korbasiewicz, E. Tijs, Direct acoustic vector field mapping: new scanning tools for measuring 3D sound intensity in 3D space, in, Proceedings of EuroNoise (2015, 2015,) 891–895.
[12] M.B. Salin, D.A. Kosteev, Nearfield acoustic holography-based methods for far field prediction, Appl. Acoust. 159 (2020) 107099, https://doi.org/10.1016/j.apacoust.2019.107099.
[13] L. Geng, X.-G. Chen, C.-D. He, W. Chen, S.-P. He, Compressive nonstationary near-field acoustic holography for reconstructing the instantaneous sound field, Mech. Syst. Sig. Process. 204 (2023) 110779, https://doi.org/10.1016/j.ymssp.2023.110779.
[14] L. Geng, X.-G. Chen, S.-P. He, C.-D. He, Reconstruction of transient acoustic field using sparse real-time near-field acoustic holography, J. Sound Vib. 568 (2024) 117973, https://doi.org/10.1016/j.jsv.2023.117973.
[15] H. Wu, Y. Zha, J. Gao, H. Zhou, N. Zhang, W. Jiang, A hybrid nearfield acoustic holography based on the mapping relationship and boundary element method, Appl. Acoust. 216 (2024) 109823, https://doi.org/10.1016/j.apacoust.2023.109823.
[16] Q. Lin, P. Wang, F. Cai, R. Zhang, Y. Mo, W. Che, Y. Li, H. Zheng, H. Zhang, Deep learning-empowered moving cascaded acoustic holography for high-fidelity and high-capacity acoustic holographic reconstruction, Appl. Acoust. 216 (2024) 109768, https://doi.org/10.1016/j.apacoust.2023.109768.
[17] J. Billingsley, R. Kinns, The acoustic telescope, J. Sound Vib. 48 (1976) 485–510, https://doi.org/10.1016/0022-460x(76)90552-6.
[18] U. Michel, History of acoustic beamforming, in, in: Proceedings of the 1st Berlin Beamforming Conference, 2006, pp. 22–23.
[19] R. Merino-Martínez, P. Sijtsma, M. Snellen, T. Ahlefeldt, J. Antoni, C.J. Bahr, D. Blacodon, D. Ernst, A. Finez, S. Funke, T.F. Geyer, S. Haxter, G. Herold, X.T. Huang, W.F. Humphreys, Q. Leclere, A.M.N. Malgoezar, U. Michel, T. Padois, A.V. Pereira, R. Gold, E. Sarradj, H. Siller, D.G. Simons, C. Spehr, A review of acoustic imaging methods using phased microphone arrays, 10 (2019) 197–230. https://doi.org/10.1007/s13272-019-00383-4.
[20] I.-J. Jung, J.-G. Ih, Design of a compact omnidirectional sound camera using the three-dimensional acoustic intensimetry, Mech. Syst. Sig. Process. 172 (2022) 108970, https://doi.org/10.1016/j.ymssp.2022.108970.
[21] T. Padois, J. Fischer, C. Doolan, O. Doutres, Acoustic imaging with conventional frequency domain beamforming and generalized cross correlation: a comparison study, Appl. Acoust. 177 (2021) 107914, https://doi.org/10.1016/j.apacoust.2021.107914.
[22] F. Ning, D. Meng, J. Wei, An improved acoustic imaging algorithm combining object detection and beamforming for acoustic camera, JASA Express Lett. 2 (2022) 064802, https://doi.org/10.1121/10.0011735.
[23] T. Iwami, K. Sawai, A. Omoto, Direction-of-arrival Estimation in half-space from Single Sample Array Snapshot, Acoust. Soc. Am 153 (2023).
[24] S. Yue, H. Hou, Method for estimating the radiated sound power of moving sound sources with linear array beamforming, Appl. Acoust. 182 (2021), https://doi.org/10.1016/j.apacoust.2021.108191.
[25] A.D. Pierce, Acoustics, Acoustical Society of America through the American Institute of Physics, 1991.
[26] M.C. Junger, D. Feit, Sound, structures, and their interaction, The Mit Press, Imp, 2010.
[27] C. Lesuer, M. Gotteland, Rayonnement Acoustique. Éléments de base, in: Rayonnement Acoustique Des Structures, y C. Lesueur Editions Eyrolles, 1988: p. Ch 3.
[28] F.J. Fahy, P. Gardonio, Sound and Structural Vibration, Elsevier, 2007.
[29] J. Rohlfing, P. Gardonio, D.J. Thompson, Comparison of decentralized velocity feedback control for thin homogeneous and stiff sandwich panels using electrodynamic proof-mass actuators, J. Sound Vib. 330 (2011) 843–867, https://doi.org/10.1016/j.jsv.2010.09.013.
[30] S.J. Elliott, M.E. Johnson, Radiation modes and the active control of sound power, J. Acoust. Soc. Am. 94 (1993) 2194–2204, https://doi.org/10.1121/1.407490.
[31] C.B. Jones, C.B. Goates, J.D. Blotter, S.D. Sommerfeldt, Experimental validation of determining sound power using acoustic radiation modes and a laser vibrometer, Appl. Acoust. 164 (2020) 107254, https://doi.org/10.1016/j.apacoust.2020.107254.
[32] I.C. Bacon, S.D. Sommerfeldt, J.D. Blotter, Developing an indirect vibration-based sound power method to determine the sound power radiated from acoustic sources, Proc. Meetings Acoust. (2022), https://doi.org/10.1121/2.0001732.
[33] P. Gardonio, R. Rinaldo, R. Del Sal, L. Dal Bo, E. Turco, A. Fusiello, Multi-view videogrammetry for the estimate of plate sound radiation. Proceedings of the 14th Intl Conference on Vibration Measurements by Laser and Noncontact Techniques, 2021.

[34] P. Gardonio, R. Rinaldo, L. Dal Bo, R. Del Sal, E. Turco, A. Fusiello, Free-field sound radiation measurement with multiple synchronous cameras, Measurement 188 (2022) 110605, https://doi.org/10.1016/j.measurement.2021.110605.
[35] P. Gardonio, G. Guernieri, E. Turco, L.D. Bo, R. Rinaldo, A. Fusiello, Reconstruction of the sound radiation field from flexural vibration measurements with multiple cameras, Mech. Syst. Sig. Process. 195 (2023) 110289, https://doi.org/10.1016/j.ymssp.2023.110289.
[36] J. Baqersad, P. Poozesh, C. Niezrecki, P. Avitabile, Photogrammetry and optical methods in structural dynamics – A review, Mech. Syst. Sig. Process. 86 (2017) 17–34, https://doi.org/10.1016/j.ymssp.2016.02.011.
[37] A.M. Wahbeh, J.P. Caffrey, S.F. Masri, A vision-based approach for the direct measurement of displacements in vibrating systems, Smart Mater. Struct. 12 (2003) 785–794, https://doi.org/10.1088/0964-1726/12/5/016.
[38] T.G. Ryall, C.S. Fraser, Determination of structural modes of vibration using digital photogrammetry, J. Aircr. 39 (2002) 114–119, https://doi.org/10.2514/2.2903.
[39] S.W. Park, H.S. Park, J.H. Kim, H. Adeli, 3D displacement measurement model for health monitoring of structures using a motion capture system, Measurement 59 (2015) 352–362.
[40] M.N. Helfrick, C. Niezrecki, P. Avitabile, T. Schmidt, 3D digital image correlation methods for full-field vibration measurement, MSSP 25 (2011) 917–927.
[41] R.S. Pappa, J.T. Black, J.R. Blandino, T.W. Jones, P.M. Danehy, A.A. Dorrington, Dot-projection photogrammetry and videogrammetry of gossamer space structures, J Spacecr Rockets 40 (2003) 858–867, https://doi.org/10.2514/2.7047.
[42] J. Javh, J. Slavič, M. Boltežar, The subpixel resolution of optical-flow-based modal analysis, Mech. Syst. Sig. Process. 88 (2017) 89–99, https://doi.org/10.1016/j.ymssp.2016.11.009.
[43] L. Yu, B. Pan, Single-camera high-speed stereo-digital image correlation for full-field vibration measurement, Mech. Syst. Signal Pr. 94 (2017) 374–383.
[44] D. Gorjup, J. Slavič, M. Boltežar, Frequency domain triangulation for full-field 3D operating-deflection-shape identification, Mech. Syst. Signal Pr. 133 (106287) (2019) 143–152.
[45] D. Gorjup, J. Slavič, A. Babnik, M. Boltežar, Still-camera multiview Spectral Optical Flow Imaging for 3D operating-deflection-shape identification, Mech. Syst. Sig. Process. 152 (2021) 107456, https://doi.org/10.1016/j.ymssp.2020.107456.
[46] J. Javh, J. Slavič, M. Boltežar, Measuring full-field displacement spectral components using photographs taken with a DSLR camera via an analogue fourier integral, Mech. Syst. Sig. Process. 100 (2018) 17–27.
[47] P.R. Stepanishen, Radiated power and radiation loading of cylindrical surfaces with nonuniform velocity distributions, J. Acoust. Soc. Am. 63 (1978) 328–338, https://doi.org/10.1121/1.381743.
[48] Y. Sun, T. Yang, Y. Chen, Sound radiation modes of cylindrical surfaces and their application to vibro-acoustics analysis of cylindrical shells, J. Sound Vib. 424 (2018) 64–77, https://doi.org/10.1016/j.jsv.2018.03.004.
[49] C.B. Goates, C.B. Jones, S.D. Sommerfeldt, J.D. Blotter, Sound power of vibrating cylinders using the radiation resistance matrix and a laser vibrometer, J. Acoust. Soc. Am. 148 (2020) 3553–3561, https://doi.org/10.1121/10.0002870.
[50] P. Gardonio, E. Turco, Tuning of vibration absorbers and Helmholtz resonators based on modal density/overlap parameters of distributed mechanical and acoustic systems, J. Sound Vib. 451 (2019) 32–70, https://doi.org/10.1016/j.jsv.2019.03.015.
[51] D.J. Ewins, Modal testing : theory, practice, and application, Research Studies Press (2000).
[52] Z. Zhang, A flexible new technique for camera calibration, IEEE Trans. Pattern Anal. Mach. Intell. 22 (2000) 1330–1334, https://doi.org/10.1109/34.888718.
[53] F. Moreno-Noguer, V. Lepetit, P. Fua, Accurate Non-Iterative O(n) Solution to the PnP Problem, in: In: 2007 IEEE 11th International Conference on Computer Vision, 2007, pp. 1–8, https://doi.org/10.1109/ICCV.2007.4409116.
[54] R. Hartley, A. Zisserman, Multiple View Geometry in Computer Vision, Cambridge University Press, 2017.
[55] R. Del Sal, L. Dal Bo, E. Turco, A. Fusiello, A. Zanarini, R. Rinaldo, P. Gardonio, Structural vibration measurement with multiple synchronous cameras, Mech. Syst. Sig. Process. 157 (2021) 107742, https://doi.org/10.1016/j.ymssp.2021.107742.
[56] B. Lucas, T. Kanade, An Iterative Image Registration Technique with an Application to Stereo Vision (IJCAI), 1981.
[57] P.M. Morse, K.U. Ingard, Theoretical Acoustics, Princeton University Press, 1986.
[58] G.H. Koopmann, J.B. Fahnline, Designing quiet structures. A sound power minimization approach, Academic Press London, 1997.
[59] E. Skudrzyk, The Foundations of Acoustics, Springer-Verlag, New York, 1971.
[60] A.W. Leissa, Vibration of Shells, Washington, 1973.
[61] S. Markus, The Mechanics of Vibrations of Cylindrical Shells, Elsevier, Oxford, 1998.
[62] W. Soedel, Vibrations of Shells and Plates, 3rd ed., CRC Press, 2004.
[63] R.D. Blevins, Formulas for Dynamics, John Wiley & Sons, Acoustics and Vibration, 2016.